Definition of a load adaptive baseline by inverse Finite Element Method for structural damage identification

L. Colombo, C. Sbarufatti, M. Giglio

Politecnico di Milano, via La Masa 1 Milano, luca1.colombo@polimi.it

Politecnico di Milano, via La Masa 1 Milano, claudio.sbarufatti@polimi.it

Politecnico di Milano, via La Masa 1 Milano, marco.giglio@polimi.it

Key Words: iFEM; Damage identification; load-adaptive baseline; Strain; Inverse problem; Data normalisation.

Abstract

One principle limitation to the implementation of Structural Health Monitoring (SHM) systems in real structures is the influence of different operational conditions with respect to those adopted during SHM system design, potentially leading to damage misclassifications. To overcome this issue, this work proposes a methodology to perform Structural Health Monitoring leveraging on the inverse Finite Element Method (iFEM). The iFEM methodology, based on the minimisation of a weighted least-squares functional defined as a comparison between the experimental strains and the corresponding numerical ones, enables the reconstruction of the strain field of a structure by means of a number of strain sensors without requiring any a-priori knowledge of the boundary load conditions. This allows providing a load-adaptive baseline based on an anomaly index that highlights the actual health state of the structure by comparing the strain reconstructed by the iFEM at some test locations with the strain measured by a test sensor in the same position, independently from the applied load and without training requirements for load cancelling. When the analysed structure is in a "healthy" condition, the two values match, otherwise they do not. If multiple test positions are considered, the damage position can also be inferred. Though the formulation of the diagnostic problem is general for an arbitrary component geometry and damage type, the proposed method is numerically demonstrated by means of a clamped plate subjected to different loads in the presence of single and multiple fatigue crack damages.

1. Introduction

In the last years scientific and industrial communities have put a lot of efforts into the development of a new framework for the assessment of structural integrity, generally known as Structural Health Monitoring (SHM), which should allow real-time, automatic evaluations of the state of the structures based on a network of permanently installed sensors, thus leading to large operative cost reductions and to the improvement of safety margins.

In general, many SHM methodologies exist in the literature, either based on data [1][2] or on models [3]. Data-based methods make use of pattern recognition or machine learning in the attempt to diagnose the structural condition from measured data without a recourse to physics-based structural models [4]. Model-based identification often considers the availability of simulated signal features for both the healthy and damaged conditions, that are used to statistically infer the most likely actual state, often based on inverse methods [5]. However, their exploitation remains limited in the industry, due to several complications which make the practical application of SHM on real structures non-trivial, the variability of operational and environmental conditions being one of the most challenging [6]. The operational load, in practice, can be naturally variable for many structures, e.g., wind-induced vibrations of aircraft wings, bridges and high-rise

buildings, and is usually an unknown input variable. In addition, the environmental conditions can markedly affect the structure's mechanical behaviour as well as the feature extraction from the recorded signals, which is carried out to perform a system's diagnosis [7][8]. As a consequence, the unseen, or the un-modeled, change of signal features might induce the SHM system to detect a damage that is actually non existing, producing a false alarm [9]. Also, changing of the operational conditions can alter the damage assessment, eventually producing a biased localisation and an overestimation (or worse, underestimation) of the damage size.

In this context, different studies are available in the literature attempting to reduce operational and environmental influences, usually referred to as data normalisation [9]. Some methods rely on regression and interpolation techniques to "learn" the dependence of any measured feature from the varying boundary condition [10][11][12][13]. However, they can only be applied if a direct measure of the varying operational parameters is available. When this measure is impractical, other methods can be used that leverage on a feature's shift, induced by damage, "orthogonal" with respect to the reference normal condition space. These include, for example, singular-value decomposition [14], principal component analysis [15], auto-associative neural networks [16], factor analysis [17] and cointegration [18][19], as a current state of the art solution. However, a common drawback of these methods is their requirement of a large amount of examples to guarantee that all the possible operational and environmental variations are considered for the algorithm training. In addition, when training is required, the algorithm performance is usually sensibly hampered outside the training domain. Finally, if the baseline condition of the system experiences a wide range of variation due to operational influences, this will hide the damage thus retarding the alarm.

In order to overcome these drawbacks, other approaches try to explicitly extract features that are mainly sensitive to damage but insensitive to environmental variations. Some of them rely on strain compatibility as a monitoring feature for damage detection [20]. The concept of strain compatibility is in fact closely related to the health state of the structure. Since the physical meaning of compatibility is the continuity of a deformed body without admitting the presence of any voids or discontinuities, the appearance of a damage in the structure leads to the violation of the strain compatibility relationship. Some works define a damage detection strategy based on this concept [21] claiming its independence on loads. Others couple the concept of strain compatibility with other techniques, like the differential equation governing plate displacements [22]. However, these approaches possess a rather localised detection area and, despite the fact they can be easily used for damage detection, their exploitation for the localisation and characterisation is quite challenging or requires displacement field measurements not easily implementable in an online system.

In this framework, a training-free methodology, the inverse Finite Element Method (iFEM), possesses some key features to overcome these issues and, at the same time, to tackle the problem of environmental and operational variability in SHM systems. The inverse Finite Element Method, originally developed by Tessler and Spangler for plate and shell structures [23][24], is receiving more and more attention in the field of shape [25][26][27] and stress sensing [28][29][30][31], in view of structural ageing assessment. While direct FEM in its basic form calculates displacements as a function of input loads and knowing the material properties, the iFEM algorithm allows reconstructing the structural displacements on the basis of some input strain measures. At a glance, it consists in minimizing in a least-squares sense a weighted error functional between measured and numerically reconstructed strains, thus finding the most likely deformed shape maximising the match with the measured strain field. As for the standard Finite Element procedure, the structure must be discretised by means of inverse elements, and a variety of solutions already exist in the literature, however limited to plate and shell-like structures [32] [33][34] and beam-like [35][36][37] ones. The advantage here is that knowledge of the applied load and the material properties is not required to reconstruct the displacements and the strain of the component, as only strain-displacement relationships are involved in the formulation [38][39]. The latter aspect can be exploited in a SHM framework, as it allows defining a load-adaptive baseline taking advantage of the algorithm ability to automatically adapt its strain field

reconstruction under different load conditions. In particular, the method is applicable to SHM systems leveraging on strain field measures [40][41], where the separation of the damage dependent signal features from the external load influence on the same signals is absolutely non-trivial [41][20].

Very few applications of the iFEM to the SHM are present in the literature, specifically for anomaly identification [42]. Thus, in this study, iFEM is used to create an anomaly index for model-based damage detection and localisation which is independent from the loading condition and which could be used to define a load-adaptive baseline for damage identification. The concept at the basis of the anomaly identification is that the iFEM algorithm will always reconstruct a strain field compatible with the healthy structure geometry, leveraging on a vector of input strain measures. If a geometrical modification occurs, which is not included in the model geometry, e.g. due to damage, it induces non-compatibility between the measured strain and the reconstructed displacements at a test position in the vicinity of the damage. In particular, we apply the method to a simple case study consisting of a clamped plate subjected to different type of loads in the presence of a fatigue crack damage, aiming to demonstrate, in a simulated scenario, the method's independence from the loading condition and to evaluate its efficacy for SHM as a function of the input sensor network layout and the mesh discretisation. The methodology is sufficiently general to be suitable for any kind of geometrical complexity (however limited to date to beam and plate like structures) and boundary conditions and is computationally efficient and fast enough for real-time implementation, involving mainly matrix-vector multiplication, both in static and dynamic applications [43][44].

The paper is structured as follows. The general iFEM framework is reviewed in Section 2, while additional information on some related mathematical aspects is collected in the Appendix. Then, the iFEM output is used in Section 3 to define an anomaly index for damage identification. Section 4 provides information on the application cases for fatigue damage diagnosis, while results are shown in Section 5 for the test cases under different load conditions, simulated in a virtual environment. A conclusive section is finally provided.

2. inverse Finite Element Method review

A detailed review of the mathematical formulation of the iFEM algorithm presented in [33] and [43] is provided in this section, explicating some passages not detailed in the literature, for the interested reader.

Suppose the structure is discretised in finite elements, as it happens for the direct FEM procedure. Without any loss of generality, this work makes use of a newly developed quadrilateral inverse-shell element, the iQS4 [33], a four-nodes inverse element based on the Mindlin theory for the kinematic definition, possessing six degrees of freedom at each node by virtue of the inclusion of drilling rotations and good stability properties, especially for membrane-like problems [45].

Differently from direct FEM which receives load as an input parameter, the iFEM formulation relies on input strain measures that are used to reconstruct the structural displacement field. In particular, the procedure for the global displacement field calculation is an optimisation problem which consists in minimizing a weighted least-squares functional that compares measured strain field components ($\cdot^{\boldsymbol{\varepsilon}}$) and a numerical formulation of the same ($\cdot\,(\boldsymbol{u})$). Note that ($\cdot\,(\boldsymbol{u})$) indicates the latter is based on the displacement field that is the implicit optimisation target. Specifically, the strain components include membrane ($\boldsymbol{e}$), bending ($\boldsymbol{k}$) and transverse shear ($\boldsymbol{g}$) deformations, associated to the inverse element mid-plane, hereafter referred to as reference plane. For each single i^{th} inverse element, the functional takes the form:

$$\Phi_i(\boldsymbol{u}^i) = w_m \left|\left|\boldsymbol{e}(\boldsymbol{u}^i) - \boldsymbol{e}_i^{\boldsymbol{\varepsilon}}\right|\right|^2 + w_b \left|\left|\boldsymbol{k}(\boldsymbol{u}^i) - \boldsymbol{k}_i^{\boldsymbol{\varepsilon}}\right|\right|^2 + w_s \left|\left|\boldsymbol{g}(\boldsymbol{u}^i) - \boldsymbol{g}_i^{\boldsymbol{\varepsilon}}\right|\right|^2 \quad (1)$$

where $\boldsymbol{u}^i$ is the vector of nodal degrees of freedom in the local coordinates and w_m, w_b, w_s are the positive valued constant parameters associated with the membrane, bending and shear strain component and control the complete coherence between numerical and experimental measures. They are particularly important in problems involving just a few measurement points and assume either a unitary value, if a measure of the specific strain component is present within the inverse element, or otherwise a small positive value.

Two features are required for the implementation of the aforementioned optimisation procedure, namely a numerical formulation for $\boldsymbol{e}$, $\boldsymbol{k}$ and $\boldsymbol{g}$ strain field components and a vector of input strain measurements ($\boldsymbol{\varepsilon_{in}}$) required for calculating $\boldsymbol{e}^{\boldsymbol{\varepsilon}}$, $\boldsymbol{k}^{\boldsymbol{\varepsilon}}$ and $\boldsymbol{g}^{\boldsymbol{\varepsilon}}$.

2.1 Kinematic framework for numerical strain formulation

As for the direct FEM, also the iFEM strategy leverages on the definition of proper coordinate reference systems to properly formulate the numerical strain field components. A local reference system (*x*, *y*, *z*) is centered in the centroid of the mid-plane quadrilateral as shown in Figure 1, and a coordinate transformation matrix ($\boldsymbol{T}^i$) from local (*x*, *y*, *z*) to global (X, Y, Z) coordinate systems is defined. The complete formulation of the transformation matrix is reported in Appendix A.

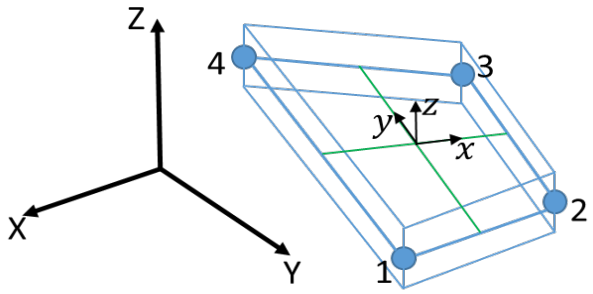

Figure 1: Local and global reference system of the iQS4 element

The shell element is assumed to have a uniform thickness *2h* with $z \in [-h; +h]$ defining the thickness coordinate, as shown later in Figure 3. The (*x*, *y*) coordinate in the reference plane are defined in (2) as a function of the bilinear shape functions $N_q(s,t)$ and the local nodal coordinates (x_q, y_q) $(q = 1,2,3,4)$ (with $(s,t) \in [-1,+1]$ being dimensionless isoparametric coordinates as shown in Figure 2).

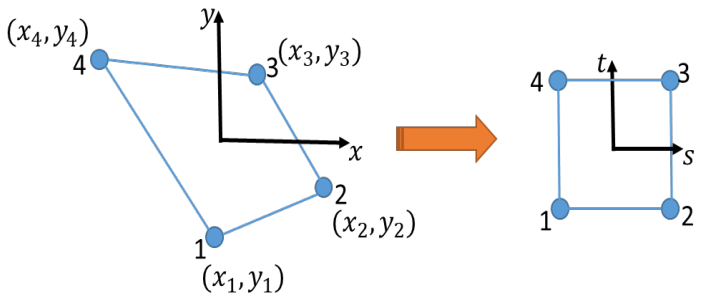

Figure 2: Local reference on the mid-plane of the element and the corresponding mapping in isoparametric coordinates

$$x(s,t) \equiv x = \sum_{q=1}^{4} N_q x_q$$
$$y(s,t) \equiv y = \sum_{q=1}^{4} N_q y_q \tag{2}$$

The explicit form of the shape functions $N_q(s,t)$ [46][47] linking the nodal displacement with the displacement of the point of interest is reported in Appendix B.

The u and v membrane displacements are defined in terms of nodal d.o.f. u_q (positive x translation), v_q (positive y translation) and θ_{zq} (rotation about the z axis) by:

$$u(x,y) \equiv u = \sum_{q=1}^{4} N_q u_q + \sum_{q=1}^{4} L_q \theta_{zq}$$
$$v(x,y) \equiv v = \sum_{q=1}^{4} N_q v_q + \sum_{q=1}^{4} M_q \theta_{zq} \tag{3}$$

with L_q and M_q shape functions defining the relation between drilling rotation d.o.f., θ_{zq}, and the membrane displacements, as discussed by Cook [46] and explicitly written in Appendix B.

The positive z translation, w_q, and the rotations about the x and y axes, θ_{xq} and θ_{yq} (positive counter clockwise), are interpolated with the anisoparametric shape functions developed by Tessler and Hughes [47] for the MIN4 element (Mindlin-type, 4 nodes) and they define, respectively, the transverse displacement w and the two bending rotations, θ_x and θ_y.

$$w(x,y) \equiv w = \sum_{q=1}^{4} N_q w_q - \sum_{q=1}^{4} L_q \theta_{xq} - \sum_{q=1}^{4} M_q \theta_{yq}$$
$$\theta_x(x,y) \equiv \theta_x = \sum_{q=1}^{4} N_q \theta_{xq} \tag{4}$$
$$\theta_y(x,y) \equiv \theta_y = \sum_{q=1}^{4} N_q \theta_{yq}$$

The components of the displacement vector at any point of the element (in-plane displacements u_x and u_y and deflection across the uniform shell thickness u_z) can be written as:

$$u_x(x,y,z) \equiv u_x = u + z\theta_y$$
$$u_y(x,y,z) \equiv u_y = v - z\theta_x \tag{5}$$
$$u_z(x,y,z) \equiv u_z = w$$

Assuming a linear elastic constitutive law and under the hypothesis of plane-stress ($\sigma_z = 0$) the transverse-normal strain ε_{zz} does not contribute to the strain energy (and for this reason it is neglected in (6)), while the other strain components can be computed as:

$$
\begin{aligned}
\varepsilon_{xx} &= \frac{\partial u_x}{\partial x} = \frac{\partial u}{\partial x} + z\frac{\partial \theta_y}{\partial x} \\
\varepsilon_{yy} &= \frac{\partial u_y}{\partial y} = \frac{\partial v}{\partial y} - z\frac{\partial \theta_x}{\partial y} \\
\gamma_{xy} &= \frac{\partial u_y}{\partial x} + \frac{\partial u_x}{\partial y} = \frac{\partial v}{\partial x} + \frac{\partial u}{\partial y} + z\left(\frac{\partial \theta_y}{\partial y} - \frac{\partial \theta_x}{\partial x}\right) \\
\gamma_{xz} &= \frac{\partial u_z}{\partial x} + \frac{\partial u_x}{\partial z} = \frac{\partial w}{\partial x} + \theta_y \\
\gamma_{yz} &= \frac{\partial u_z}{\partial y} + \frac{\partial u_y}{\partial z} = \frac{\partial w}{\partial y} - \theta_x
\end{aligned}
\tag{6}
$$

It is worth noticing that the derivatives in the previous equations, involve the computation of the partial derivatives of the shape functions with respect to x and y coordinates. The Jacobian operator is required for this computation, whose explicit form is given in Appendix C.
Finally, introducing Eqs.(3) and (4) into Eq. (6), it is possible to express the strain-displacement relations as a function of the element nodal displacement vector $\boldsymbol{u}^i$ and to divide them into membrane, bending and transverse shear strains $\boldsymbol{e}(\boldsymbol{u}^i), \boldsymbol{k}(\boldsymbol{u}^i), \boldsymbol{g}(\boldsymbol{u}^i)$ respectively, leading to Eqs. (7) and (8).

$$
\begin{aligned}
\boldsymbol{e}(\boldsymbol{u}^i) &= \boldsymbol{B^m}\boldsymbol{u}^i \\
\boldsymbol{k}(\boldsymbol{u}^i) &= \boldsymbol{B^b}\boldsymbol{u}^i \\
\boldsymbol{g}(\boldsymbol{u}^i) &= \boldsymbol{B^s}\boldsymbol{u}^i
\end{aligned}
\tag{7}
$$

$$
\begin{aligned}
\begin{Bmatrix} \varepsilon_{xx} \\ \varepsilon_{yy} \\ \gamma_{xy} \end{Bmatrix} &\equiv \boldsymbol{e}(\boldsymbol{u}^i) + z\boldsymbol{k}(\boldsymbol{u}^i) \\
\begin{Bmatrix} \gamma_{xz} \\ \gamma_{yz} \end{Bmatrix} &\equiv \boldsymbol{g}(\boldsymbol{u}^i)
\end{aligned}
\tag{8}
$$

where *z* is, again, the local through-the-thickness coordinate, while the matrices $\boldsymbol{B^m}$, $\boldsymbol{B^b}$, $\boldsymbol{B^s}$ contain the derivatives of the shape functions governing the membrane, bending and shear structural response, respectively and their explicit expressions are reported in Appendix B. Finally, the vector $\boldsymbol{u}^i$ is expressed as:

$$
\begin{aligned}
\boldsymbol{u}^i &= \left[\boldsymbol{u_1^i}\ \boldsymbol{u_2^i}\ \boldsymbol{u_3^i}\ \boldsymbol{u_4^i}\right]^T \\
\boldsymbol{u_q^i} &= \left[u_q\ v_q\ w_q\ \theta_{xq}\ \theta_{yq}\ \theta_{zq}\right]^T\ (q = 1,2,3,4)
\end{aligned}
\tag{9}
$$

2.2 Definition of the experimental strain vector

The most general iFEM definition allows considering n discrete measure positions $\boldsymbol{x}_j = (x_j, y_j, \pm h)(j = 1, \dots, n)$ within each element and no limitation is posed about the sensor type, which can be, for instance, a strain rosette measuring multiple strain tensor components, as ε_{xx}, ε_{yy} and ε_{xy}, with x and y being the local coordinate axes. However, the method requires a proper sensor configuration in order to capture and distinguish membrane, bending and shear strain components. If only surface measurements are allowed, like in the majority of the engineering problems, the membrane and bending strain contributions can be evaluated as in Eq. (10) if a measure is taken at both free surfaces of the plate component (Figure 3), thus at $\pm\, h$ distance from the midplane:

$$\boldsymbol{e}_{i,j}^{\boldsymbol{\varepsilon}} = \frac{1}{2}\begin{Bmatrix} \varepsilon_{xx}^{+} + \varepsilon_{xx}^{-} \\ \varepsilon_{yy}^{+} + \varepsilon_{yy}^{-} \\ \gamma_{xy}^{+} + \gamma_{xy}^{-} \end{Bmatrix}_{i,j} \quad (j = 1, \dots, n)$$
$$\boldsymbol{k}_{i,j}^{\boldsymbol{\varepsilon}} = \frac{1}{2h}\begin{Bmatrix} \varepsilon_{xx}^{+} - \varepsilon_{xx}^{-} \\ \varepsilon_{yy}^{+} - \varepsilon_{yy}^{-} \\ \gamma_{xy}^{+} - \gamma_{xy}^{-} \end{Bmatrix}_{i,j} \tag{10}$$

where the superscript '+' and '-' denote the strain measured on the top and bottom surfaces, respectively. The transverse shear strains $\boldsymbol{g}^{\boldsymbol{\varepsilon}}$ cannot be directly computed from surface strains. However, even though some procedures exist for computing transverse shear strains from the bending strains [48][49], they can be reasonably discarded in the formulation since they contribute to the deformation, in thin shells, to a much smaller extend compared to the bending curvature. Finally, the iFEM does not require a one-to-one instrumentation, i.e. not all the elements of the structure must be instrumented with strain sensors. If no measure is associated to some elements, the associated $\boldsymbol{e}^{\boldsymbol{\varepsilon}}$, $\boldsymbol{k}^{\boldsymbol{\varepsilon}}$ and $\boldsymbol{g}^{\boldsymbol{\varepsilon}}$ is null, however with a small related weight w_m, w_b, w_s.

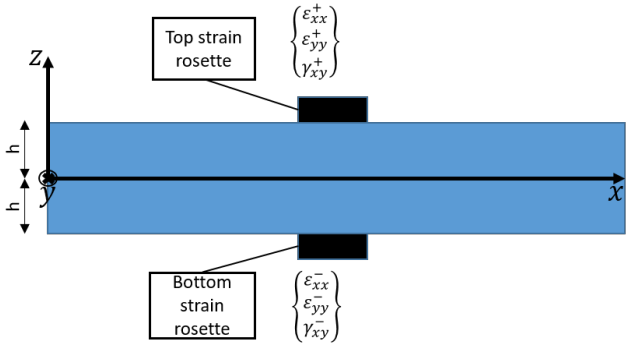

Figure 3: Discrete positions of strain rosettes

2.3 Displacement calculation by a weighted least-squares variational formulation

As described before, the iFEM relies on the minimisation of a global weighted least-squares functional, Φ, taking into account the contribution of each n_{el} inverse elements defined as:

$$\Phi = \sum_{i=1}^{n_{el}} \Phi_i(\boldsymbol{u}^i) \tag{11}$$

in which every Φ_i functional, with i referring to the element considered, takes the form specified in Eq. (1). In particular, for elements including at least one experimental strain measure, the squared norms in Eq. (1) can be expressed in terms of normalised Euclidean norms as:

$$\left|\left|\boldsymbol{e}(\boldsymbol{u}^i) - \boldsymbol{e}_i^{\boldsymbol{\varepsilon}}\right|\right|^2 = \frac{1}{n}\iint_{A_i} \sum_{j=1}^{n} \left(\boldsymbol{e}(\boldsymbol{u}^i)_j - \boldsymbol{e}_{i,j}^{\boldsymbol{\varepsilon}}\right)^2 dxdy$$
$$\left|\left|\boldsymbol{k}(\boldsymbol{u}^i) - \boldsymbol{k}_i^{\boldsymbol{\varepsilon}}\right|\right|^2 = \frac{(2h)^2}{n}\iint_{A_i} \sum_{j=1}^{n} \left(\boldsymbol{k}(\boldsymbol{u}^i)_j - \boldsymbol{k}_{i,j}^{\boldsymbol{\varepsilon}}\right)^2 dxdy \tag{12}$$
$$\left|\left|\boldsymbol{g}(\boldsymbol{u}^i) - \boldsymbol{g}_i^{\boldsymbol{\varepsilon}}\right|\right|^2 = \frac{1}{n}\iint_{A_i} \sum_{j=1}^{n} \left(\boldsymbol{g}(\boldsymbol{u}^i)_j - \boldsymbol{g}_{i,j}^{\boldsymbol{\varepsilon}}\right)^2 dxdy$$

where A_i is the mid-plane area of the i^{th} element.

There is also the possibility to use "measure-less" inverse elements, meaning elements with missing experimental measures. In this case, the corresponding norm in Eq. (12) is substituted by its reduced form:

$$\begin{aligned}\left|\left|\boldsymbol{e}(\boldsymbol{u}^i)\right|\right|^2 &= \iint_{A_i} \left(\boldsymbol{e}(\boldsymbol{u}^i)\right)^2 dxdy \\ \left|\left|\boldsymbol{k}(\boldsymbol{u}^i)\right|\right|^2 &= (2h)^2 \iint_{A_i} \left(\boldsymbol{k}(\boldsymbol{u}^i)\right)^2 dxdy \\ \left|\left|\boldsymbol{g}(\boldsymbol{u}^i)\right|\right|^2 &= \iint_{A_i} \left(\boldsymbol{g}(\boldsymbol{u}^i)\right)^2 dxdy\end{aligned} \tag{13}$$

For such elements, all the integrals in Eq. (13) are multiplied by small weighting constants $w_m = w_b = w_s = \alpha = 10^{-4}$. This allows maintaining the necessary connectivity between the elements having strain-sensor data even in case of very sparse measured quantities.
After some mathematical passages, the functional in Eq. (1) can be written as:

$$\Phi_i(\boldsymbol{u}^i) = \boldsymbol{u}^{i^T}\boldsymbol{k}^i\boldsymbol{u}^i - 2\boldsymbol{u}^{i^T}\boldsymbol{f}^i + \xi^i \tag{14}$$

in which:

$$\begin{aligned}\boldsymbol{k}^i &= \iint_{A_i} (w_m \boldsymbol{B}^{\boldsymbol{m}^T}\boldsymbol{B}^{\boldsymbol{m}} + w_b(2h)^2\boldsymbol{B}^{\boldsymbol{b}^T}\boldsymbol{B}^{\boldsymbol{b}} + w_s\boldsymbol{B}^{\boldsymbol{s}^T}\boldsymbol{B}^{\boldsymbol{s}})dxdy \\ \boldsymbol{f}^i &= \frac{1}{n}\iint_{A_i}\sum_{j=1}^{n}\left(w_m\boldsymbol{B}^{\boldsymbol{m}^T}\boldsymbol{e}^{\boldsymbol{\varepsilon}}_{i,j} + w_b(2h)^2\boldsymbol{B}^{\boldsymbol{b}^T}\boldsymbol{k}^{\boldsymbol{\varepsilon}}_{i,j} + w_s\boldsymbol{B}^{\boldsymbol{s}^T}\boldsymbol{g}^{\boldsymbol{\varepsilon}}_{i,j}\right)dxdy \\ \xi^i &= \frac{1}{n}\iint_{A_i}\sum_{j=1}^{n}\left(w_m\boldsymbol{e}^{\boldsymbol{\varepsilon}}_{i,j}{}^T\boldsymbol{e}^{\boldsymbol{\varepsilon}}_{i,j} + w_b(2h)^2\boldsymbol{k}^{\boldsymbol{\varepsilon}}_{i,j}{}^T\boldsymbol{k}^{\boldsymbol{\varepsilon}}_{i,j} + w_s\boldsymbol{g}^{\boldsymbol{\varepsilon}}_{i,j}{}^T\boldsymbol{g}^{\boldsymbol{\varepsilon}}_{i,j}\right)dxdy\end{aligned} \tag{15}$$

Notice that, in the expression of the functional Φ_i of Eq. (14), the term ξ^i is independent of the element nodal displacement vector $\boldsymbol{u}^i$, thus, will be deleted in the following minimisation process. Furthermore, the $\boldsymbol{f}^i$ vector is function both of the number and values of the measurement strains within the element, while the matrix $\boldsymbol{k}^i$ is independent of the measured strain values.
So far, all the computations were carried out in local coordinate. Now, consider the element displacement vector in global coordinates

$$\boldsymbol{U}^i = \boldsymbol{T}^i\boldsymbol{u}^i \tag{16}$$

in which $\boldsymbol{T}^i$ is, again, the transformation matrix from local to global coordinates in Appendix A, and an extraction matrix $\boldsymbol{E}_i$ of the element *i* such that

$$\boldsymbol{U}^i = \boldsymbol{E}_i\boldsymbol{U} \tag{17}$$

where $\boldsymbol{U}$ is the global displacement vector. By applying standard finite element procedures for assembling the contribution of each inverse element in a global system, $\Phi(\boldsymbol{u}^1, \boldsymbol{u}^2, \dots, \boldsymbol{u}^{n_{el}}) \rightarrow \Phi(\boldsymbol{U})$, the global functional of Eq. (11) is reduced to

$$\Phi(\boldsymbol{U}) = \boldsymbol{U}^{\boldsymbol{T}}\boldsymbol{K}\boldsymbol{U} - 2\boldsymbol{U}^{\boldsymbol{T}}\boldsymbol{F} + \Xi \tag{18}$$

With

$$\boldsymbol{K} = \sum_{i=1}^{n_{el}} \boldsymbol{E}_i^T \boldsymbol{T}^{i^T} \boldsymbol{k}^i \boldsymbol{T}^i \boldsymbol{E}_i$$
$$\boldsymbol{F} = \sum_{i=1}^{n_{el}} \boldsymbol{E}_i^T \boldsymbol{T}^{i^T} \boldsymbol{f}^i \tag{19}$$
$$\Xi = \sum_{i=1}^{n_{el}} \xi^i$$

Minimizing the global weighted functional of Eq. (18) with respect to the global displacements vector of the structure $\boldsymbol{U}$, the global system of equations can be obtained:

$$\frac{\partial \Phi(\boldsymbol{U})}{\partial \boldsymbol{U}} = \boldsymbol{K}\boldsymbol{U} - \boldsymbol{F} = 0 \tag{20}$$

or simply

$$\boldsymbol{K}\boldsymbol{U} = \boldsymbol{F} \tag{21}$$

where $\boldsymbol{K}$ is a symmetric matrix independent on the measured data, while $\boldsymbol{F}$ is a vector function of the measured strain values. However, the matrix $\boldsymbol{K}$ is singular, since it includes the rigid body motion of the structure. Thus, by imposing the displacement boundary conditions, Eq. (21) can be reduced to:

$$\boldsymbol{K_{FF}}\boldsymbol{U_F} = \boldsymbol{F_F} \tag{22}$$

where $\boldsymbol{K_{FF}}$ is a positive definite matrix always non-singular, assuring that a solution of the system exists, and including only the contribution of the unconstrained degrees of freedom. Since the matrix $\boldsymbol{K_{FF}}$ only depends on the sensor layout and the considered mesh discretisation, it only needs to be calculated (and inverted) once, off-line, leading to a computational very efficient real-time operation of the algorithm. On the other hand, the vector $\boldsymbol{F_F}$ is dependent on the measured strain values $\boldsymbol{\varepsilon_{in}}$ and, thus, it needs to be updated at each time step during assessment.

After the global displacement field is calculated as $\boldsymbol{U_F} = \boldsymbol{K_{FF}}^{-1}\boldsymbol{F_F}$, the reconstructed strain field, hereafter referred to as $\boldsymbol{\varepsilon_{iFEM}}$ and satisfying the strain-displacement compatibility, is computed through Eq. (8), the latter expressed in the local reference system. A model M_{iFEM} is thus available for real-time calculation of $\boldsymbol{\varepsilon_{iFEM}}$ as a function of $\boldsymbol{\varepsilon_{in}}$.

3. iFEM exploitation for damage identification

Numerical methods, including both direct and inverse FEM strategies, rely on the knowledge of the exact structure geometry, on which the mesh element layout and the nodal connectivity depend. A geometrical discrepancy with respect to the real structure is usually reflected in an erratic displacement prediction, thus in non-compatibility of the numerically reconstructed displacement field with an eventual measure taken by a test sensor. The latter consideration is exploited hereafter for anomaly identification. Given a discretised model of a healthy structure exists, any structural anomaly can be identified by means of a comparison between the numerically simulated strains and those measured by sensors at the same positions (Figure 4). Whenever the real structure is in a healthy condition the two values should match while, if the real structure is damaged (e.g. by a fatigue crack, bullet perforation, wear, etc.), the two values differ. The greater the difference, the higher the probability that the damage is located in the proximity of the sensor. By taking advantage of this observation it is possible, given a sensor grid is present within the structure, to discern between healthy and damaged conditions and in case of damage to localise it.

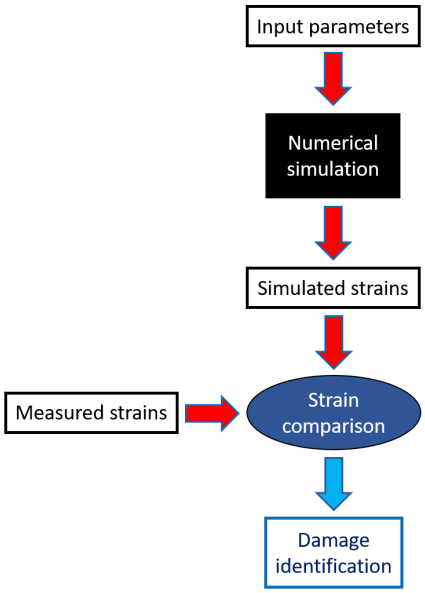

Figure 4: Strain based anomaly detection scheme

Referring to Figure 4, simulation tasks can be performed exploiting either a direct or inverse FEM analysis. If direct FEM is considered, two fundamental inputs are the material properties and the loads acting on the structure at every time instant considered. However, the latter are not always available. In particular, concerning the loads, neither their exact points of application nor their magnitude and shape are easily measurable, especially with some particular types of loads including the aerodynamic load. In this framework, the advantages of the iFEM strategy, compared to a direct FEM, are evident, as detailed in Table 1. Above all, the iFEM allows calculating the displacement field $\boldsymbol{U}$ and the strain field $\boldsymbol{\varepsilon_{iFEM}}$ without knowing the input loads and the material properties, provided a sufficient number of strain measures are available as input, which is the case for some engineering problems. Furthermore, if compared to the direct FEM, the iFEM algorithm is much more computationally efficient for real-time implementation. iFEM results are in fact readily available after each strain observation since the global strain field $\boldsymbol{\varepsilon_{iFEM}}$ computation does not require any matrix inversion.

	Direct FEM	**iFEM**
Material properties	Required	Not required (for displacement and strain field reconstruction)
Input	Force/pressure distribution	Discrete strain measures
Real time performance	High computational requirements	Results (displacement/strain reconstruction) readily available

Table 1: Comparison between direct FEM and iFEM for anomaly identification

3.1 Definition of an index for anomaly identification

Leveraging on the previously stated benefits of the iFEM, a synthetic index is defined in this section, which can be used to classify the structural health state and to locate the damaged area.

Damage identification is based hereafter on the assumption that a defect alters the strain field of the monitored structure.

To this end, consider a generic plate structure is subjected to a generic load as depicted in Figure 5 and assume the iFEM structural model M_{iFEM} is available. The plate is defined on a domain Ω of the form:

$$\Omega = \{(x, y, z) \in \mathbb{R}^3; z \in [-h; +h], (x, y) \in \mathbb{R}^2 \subset A\}$$

where A is the mid-plane area.

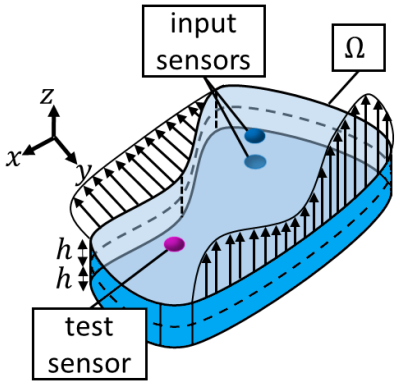

Figure 5: Plate structure subjected to a generic load, with indicated generic test and input sensor positions.

Furthermore, suppose a pattern of measured input strains $\boldsymbol{\varepsilon_{in}} \in \mathbb{R}^{n_{in} \times n_{st,in}}$ is available at the input sensor positions $\boldsymbol{x_{in}} \in \mathbb{R}^{n_{in} \times 3} \wedge x_{in} \subset \Omega$, where n_{in} is the number of the input strain sensor positions and $n_{st,in}$ is the number of the strain tensor components measured at $\boldsymbol{x_{in}}$. A pattern of test strain measures $\boldsymbol{\varepsilon_t} \in \mathbb{R}^{n_t \times n_{st,t}}$ is also available at the test strain sensor positions $\boldsymbol{x_t} \in \mathbb{R}^{n_t \times 3} \wedge x_t \subset \Omega$, where n_t is the number of test strain sensor positions and $n_{st,t}$ is the number of strain tensor components measured at $\boldsymbol{x_t}$.

$\boldsymbol{\varepsilon_{in}}$ is passed as input to the iFEM model M_{iFEM} simulating the global strain field of the entire structure, from which the simulated strain response at $\boldsymbol{x_t}$ is collected into $\boldsymbol{\varepsilon_{iFEM}} \in \mathbb{R}^{n_t \times n_{st,t}}$.

$$\boldsymbol{\varepsilon_{iFEM}} = M_{iFEM}(\boldsymbol{\varepsilon_{in}}) \in \mathbb{R}^{n_t \times n_{st,t}} \tag{23}$$

Anomaly identification is performed hereafter comparing the reconstructed strain response $\boldsymbol{\varepsilon_{iFEM}}$ with the test strain measures $\boldsymbol{\varepsilon_t}$.

In the most general case, six strain tensor components are available at each test location, $\mathbb{R}^{n_t \times n_{st,t}} \equiv \mathbb{R}^{n_t \times 6}$. Thus, an equivalent strain is used to condensate in a synthetic variable all the strain information available at each test sensor position ε_{eq}: $\mathbb{R}^{n_t \times n_{st,t}} \rightarrow \mathbb{R}^{n_t \times 1}$, allowing the comparison to be carried out in a space $\mathbb{R}^{n_t \times 1}$. In order to discard any dependence from the selected reference system, an equivalent strain proportional to the second invariant of the deviatoric strain tensor [50] is selected, which synthetises shape changes at a constant volume and takes the form:

$$\varepsilon_{eq} = \frac{1}{\sqrt{2}} \cdot \sqrt{\left(\varepsilon_{xx} - \varepsilon_{yy}\right)^2 + (\varepsilon_{xx} - \varepsilon_{zz})^2 + \left(\varepsilon_{yy} - \varepsilon_{zz}\right)^2 + 6 \cdot (\gamma_{xy}^2 + \gamma_{xz}^2 + \gamma_{yz}^2)} \tag{24}$$

However, a plane strain measure is usually available in most engineering problems, e.g. allowing the calculation of $\varepsilon_{xx}, \varepsilon_{yy}$ and γ_{xy} strain tensor components if a strain rosette is used. In this case, the equivalent strain takes the reduced form, $\varepsilon_{eq}: \mathbb{R}^3 \rightarrow \mathbb{R}^1$:

$$\varepsilon_{eq} = \frac{1}{\sqrt{2}} \cdot \sqrt{\left(\varepsilon_{xx} - \varepsilon_{yy}\right)^2 + \varepsilon_{xx}^2 + \varepsilon_{yy}^2 + 6\gamma_{xy}^2} \tag{25}$$

For the sake of clarity, no assumption has been made about the out of plane strain components. The reduced form of the equivalent strain only refers to the fact that the strain rosette sensor only measures the surface in-plane strain components.

Finally, after evaluating ε_{eq} at $\boldsymbol{x_t}$ positions based on $\boldsymbol{\varepsilon_t}$ and $\boldsymbol{\varepsilon_{iFEM}}$, obtaining $\boldsymbol{\varepsilon_{eq,t}} \in \mathbb{R}^{n_t}$ and $\boldsymbol{\varepsilon_{eq,iFEM}} \in \mathbb{R}^{n_t}$ respectively, the anomaly index is evaluated for each test sensor position $x_t \subset \boldsymbol{x_t}$ as the percentage difference between the equivalent measured strain in x_t, $\varepsilon_{eq,t}$, and the one reconstructed by the iFEM in the same position, $\varepsilon_{eq,iFEM}$:

$$i(x_t) = \frac{\varepsilon_{eq,t}(x_t) - \varepsilon_{eq,iFEM}(x_t)}{\varepsilon_{eq,t}(x_t)} \cdot 100 \tag{26}$$

The anomaly index defined in Eq. (26) holds the following properties:

- It condenses a tensorial strain variable into a scalar, specifically $\mathbb{R}^3 \rightarrow \mathbb{R}^1$
- It is independent from the strain sensor reference system
- It is independent from the magnitude of the applied load

Whenever the structure is in a healthy state, the vector $\boldsymbol{i}(\boldsymbol{x_t}) \in \mathbb{R}^{n_t}$ of the anomaly indices defined in Eq. (26) is expected to result in a null vector, meaning $\boldsymbol{\varepsilon_{iFEM}}$ coincides with $\boldsymbol{\varepsilon_t}$ at each test sensor position $x_t \subset \boldsymbol{x_t}$. On the contrary, if the structure is damaged, some values in the vector $\boldsymbol{i}(\boldsymbol{x_t})$ will deviate from zero for the test positions close to the defect, due to non-compatibility of $\boldsymbol{\varepsilon_t}$ with the displacement field reconstructed by the iFEM, $\boldsymbol{U}$.

In the following, we discuss how the anomaly index in Eq. (26) is used to define a baseline, which is also insensitive to the type of boundary load condition, subsequently verifying the method performance in the results section.

3.2 Independence from the modelled loading boundary condition

It is widely recognised in the SHM literature that different loading conditions potentially induce health condition misclassifications due to baseline modifications, especially when strain field based diagnosis is involved. In this framework, the iFEM numerically propagates the strain measured at input sensor positions $\boldsymbol{x_{in}}$ to some test positions $\boldsymbol{x_t}$, taking into consideration the actual load the structure undergoes. If a proper damage index is defined that compares the iFEM strain predictions with the strain measures from some test sensors, a constant baseline pattern of anomaly indices $\boldsymbol{i}(\boldsymbol{x_t})$ is maintained regardless of the load or combination of loads are acting on the structure. The baseline is thus adapted in real time to the acting load without any requirement for algorithm training.

A schematic representation of the working mechanism is shown in Figure 6. Suppose a varying boundary load is applied to the healthy structure at discrete time steps $l_1, l_2, \dots, l_k, \dots, l_{end}$. At time step k, the generic load condition l_k generates a unique strain field which affects both the input strain measures $\boldsymbol{\varepsilon_{in_k}}$ and the test measures $\boldsymbol{\varepsilon_{t_k}}$. The former is passed as input to the iFEM model $M_{iFEM}(\boldsymbol{\varepsilon_{in_k}})$, then calculating $\boldsymbol{\varepsilon_{eq,iFEM_k}}$, while the latter is directly used for calculating $\boldsymbol{\varepsilon_{eq,t_k}}$. The comparison between these two quantities results in the

vector of the anomaly indices in Eq. (26). If the healthy structure is considered, the following identity can be derived $\boldsymbol{\varepsilon_{eq,iFEM_k}} = \boldsymbol{\varepsilon_{eq,t_k}}$, thus $\boldsymbol{i}_k = \mathbf{0}\ \forall\ k \in \mathbb{N}$, under the following rather ideal assumptions:

1. The contribution of $\boldsymbol{g^{\varepsilon}}$ is negligible, which is verified for most of the engineering applications involving plate-shell components [33].
2. No limitations are posed with regards to the number of inverse elements, n_{el}
3. One to one instrumentation: each n_{el} inverse element is instrumented with a strain rosette, acquiring 3 strain tensor components for each element (i.e. $\varepsilon_{xx}, \varepsilon_{yy}, \gamma_{xy}$)
4. The model represents with high fidelity the real structure geometry and boundary conditions
5. No noise is present in the both the input $\boldsymbol{\varepsilon_{in_k}}$ and test $\boldsymbol{\varepsilon_{t_k}}$ strain measures

These hypotheses are however not even remotely met in realistic applications, and sensitivity analysis on those influencing factors is mandatory. In particular, in the following the focus is drawn on testing the method when conditions 2 and 3 do not apply, verifying the method performance for different mesh discretisations, thus limiting n_{el}, and using a different number of input sensors, thus limiting n_{in}. As for the violation of conditions 4 and 5, although not considered here for brevity, some studies in the literature claim that the iFEM is capable to cope with small errors in the modelled geometry and noised input strain measures [51].

Violation of all these hypothesis will always induce errors in the strain field reconstruction by the iFEM, implying $\boldsymbol{i}_k \neq \mathbf{0}$ for the healthy structure. In this case, one can collect some example patterns of the baseline, i.e. taking into account a realistic sensor layout, noise and uncertainty, then applying novelty detection schemes for outlier identification, e.g. based on Mahalanobis distance [52], as well as data normalisation to improve the diagnostic accuracy. While the literature on novelty identification [4] and data normalisation [9] is vast, for brevity and without any loss of generality, the feature extraction performance under different boundary load conditions is demonstrated below.

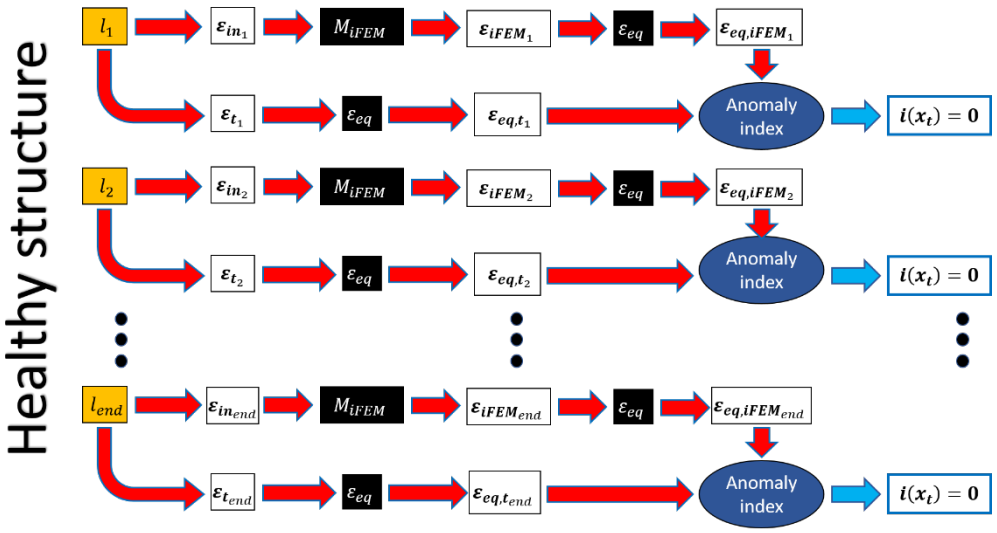

Figure 6: Workflow of the adaptive baseline

4. Case study

4.1 The specimen

The approach for damage identification is tested on a cantilever plate subjected to different loading conditions. The plate has a length of 150 mm, a width of 60 mm and a thickness of 5 mm (Figure 7).

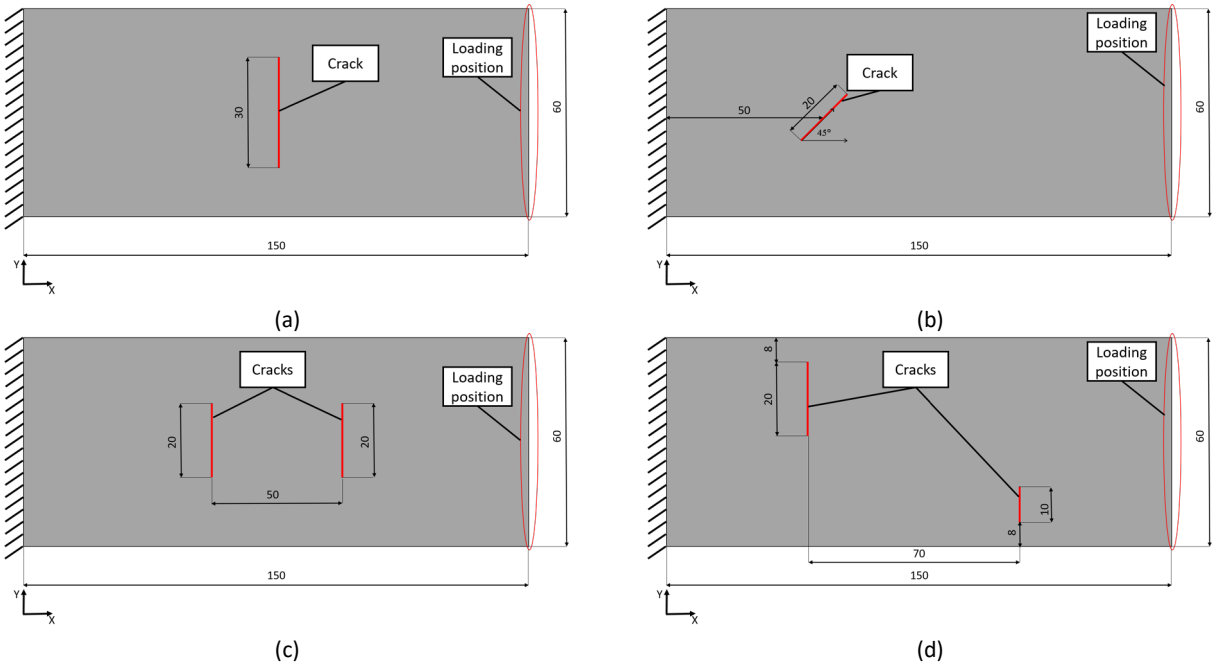

Figure 7: Plate dimensions(mm), boundary conditions and crack positions; (a) $30\ mm$ crack oriented at 90 degrees with respect to the lateral edges; (b) $20\ mm$ crack oriented at 45 degrees with respect to the lateral edges; (c) Two $20\ mm$ cracks oriented at 90 degrees with respect to the lateral edges; (d) Two cracks ($20\ mm$ and $10\ mm$ respectively) oriented at 90 degrees with respect to the lateral edges.

The plate is made of Aluminium with an elastic modulus of $79\ GPa$ and a Poisson's ratio of 0.33. Four load conditions are applied at the free end of the plate:

1. Load in the positive X direction, with a magnitude of $600\ N$, simulating plate tension
2. Load in the negative Z direction, with a magnitude of $60\ N$, simulating plate bending
3. Torque in the positive X direction, with a magnitude of $120\ Nmm$
4. A combination of the previous loads: load in the positive X direction and in the negative Z direction ($120\ N$ each) and a torque in the positive X direction ($120\ Nmm$)

Four different damaged scenarios are considered for verification purposes, the first two consisting in a plate with a single crack damage, and the others including multiple-site damages. Specifically, the first scenario consists in a damaged plate with a $30\ mm$ crack located in the middle of the plate, as shown in Figure 7a; the second is a plate with a $20\ mm$ crack oriented at 45 degrees and positioned at $50\ mm$ from clamp, as in Figure 7b; the third scenario is a plate with two $20\ mm$ long cracks spaced by $50\ mm$, as in Figure 7c, while the fourth is a plate with two cracks spaced by $70\ mm$ and with a length of $20\ mm$ and $10\ mm$ respectively, as shown in Figure 7.

4.2 The direct FEM for strain measure simulation

As described in Section 3, damage identification is based on a comparison of the strain measured at some locations with the strain reconstructed by the iFEM. In this study, we demonstrate the applicability of the damage identification method with simulated strain measures. Both the strain measures as input to the iFEM ($\boldsymbol{\varepsilon_{in}}$) and those used for the damage index calculation ($\boldsymbol{\varepsilon_t}$) are numerically simulated with a FE model of the plate in Figure 7. The latter is created in ABAQUS and consists in a high-fidelity mesh composed by 9000 S4 shell elements. Fatigue crack damage is introduced using the SEAM feature available in ABAQUS, thus duplicating nodes along the crack edge and allowing crack opening when load is applied.

The FE model is used to generate strain patterns both in healthy and damaged states and with different loading conditions, followed by the evaluation of the different responses of the method when the numerically simulated strain measures are used as input to the iFEM. An example of the strain pattern and the deformed configuration simulated for each loading condition is reported in Figure 8 and Figure 9. For brevity, no noise is used in this work to corrupt the input measures, however the influence of noise on the anomaly identification is a mandatory investigation for future activities due to the intrinsic noisy nature of real strain measures. However, some works are available in the literature verifying the iFEM robustness against noisy measurements [51]. In fact, even in the presence of noisy strain measures, intrinsic smoothing operations are included in the iFEM procedure, facilitating an accurate displacement field reconstruction by the algorithm [53].

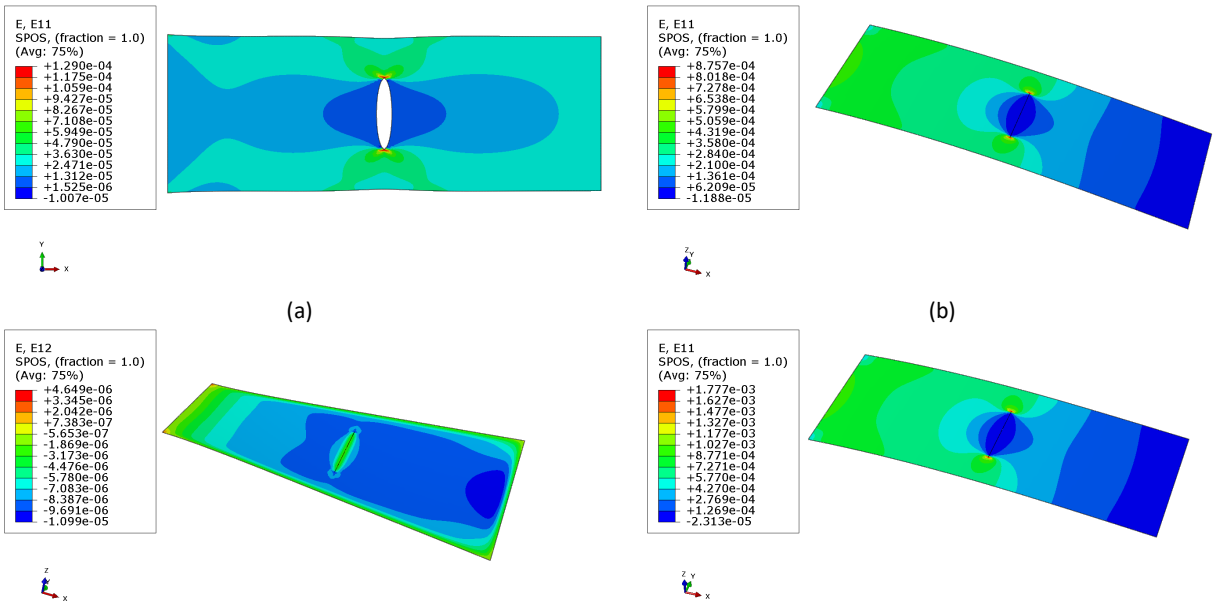

Figure 8: Strain field with different loading conditions and the crack oriented as in Figure 7a; (a) Strain field E11 with the loading condition 1; (b) Strain field E11 with the loading condition 2; (c) Strain field E12 with the loading condition 3; (d) Strain field E11 with the loading condition 4

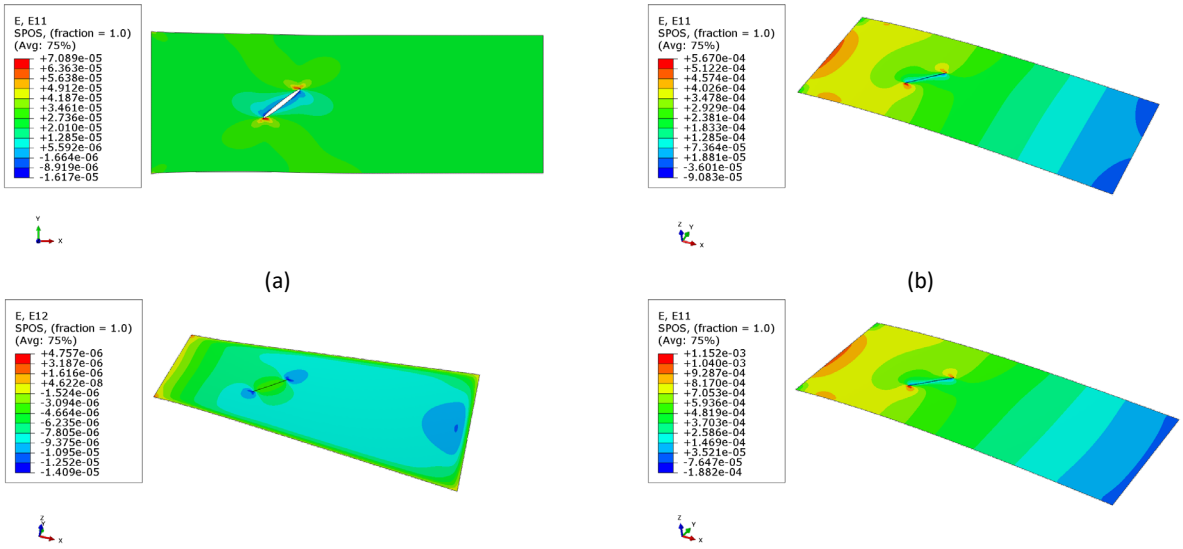

Figure 9: Strain field with different loading conditions and the crack oriented as in Figure 7b; (a) Strain field E11 with the loading condition 1; (b) Strain field E11 with the loading condition 2; (c) Strain field E12 with the loading condition 3; (d) Strain field E11 with the loading condition 4

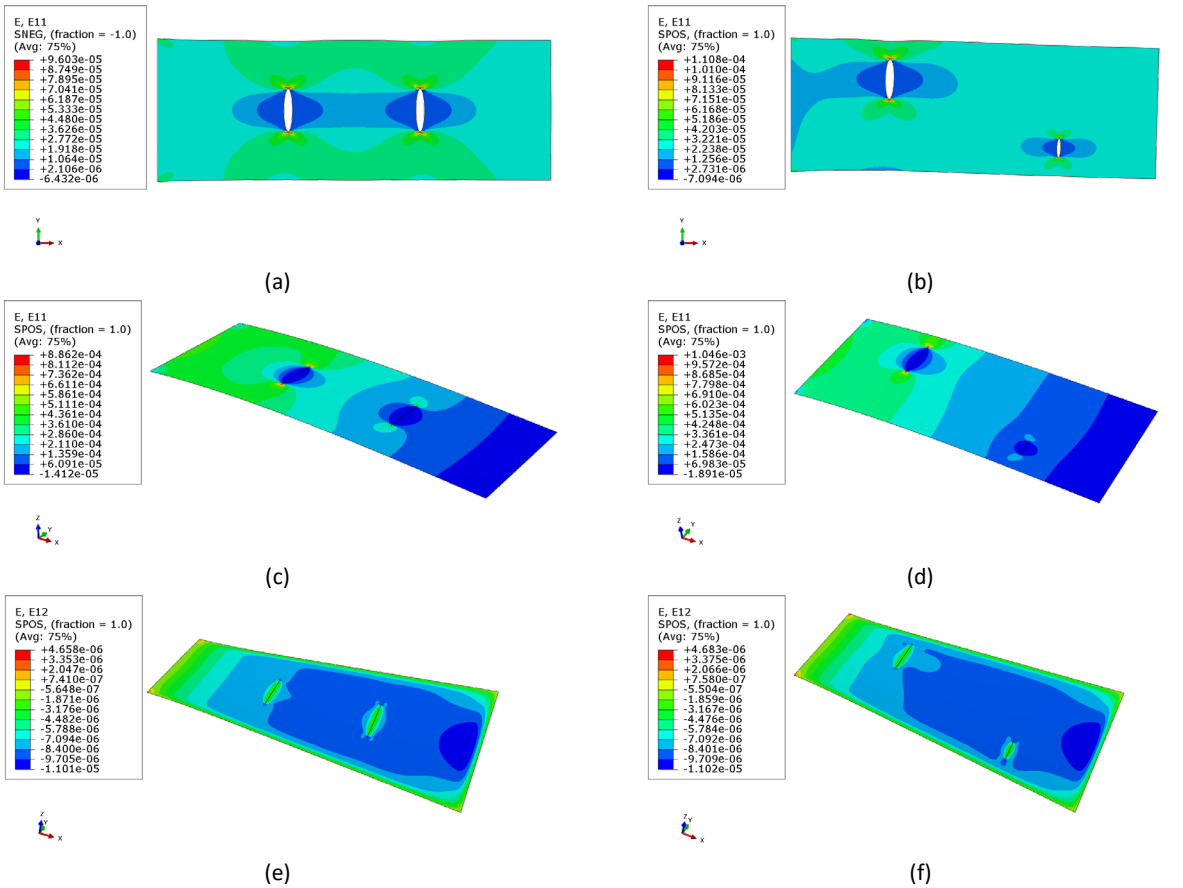

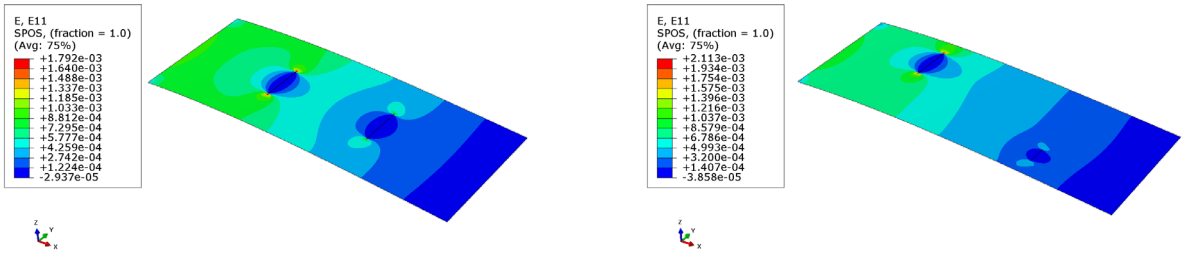

(g) (h)

Figure 10: Strain field with different loading conditions and two cracks oriented as in Figure 7c and Figure 7d; (a) Strain field E11 with the loading condition 1 and the two cracks as in Figure 7c; (b) Strain field E11 with the loading condition 1 and the two cracks as in Figure 7d; (c) Strain field E11 with the loading condition 2 and the two cracks as in Figure 7c; (d) Strain field E11 with the loading condition 2 and the two cracks as in Figure 7d; (e) Strain field E12 with the loading condition 3 and the two cracks as in Figure 7c; (f) Strain field E12 with the loading condition 3 and the two cracks as in Figure 7d; (g) Strain field E11 with the loading condition 4 and the two cracks as in Figure 7c (h) Strain field E11 with the loading condition 4 and the two cracks as in Figure 7d.

4.3 The inverse FEM for strain reconstruction and damage identification

Since it is widely recognised that the iFEM allows obtaining a good reconstruction of the displacement fields though with a less refined mesh [54], the same plate structure is discretised with a coarse mesh composed by 360 inverse elements, thus requiring less computational effort in view of a real-time implementation of the method. As anticipated in Section 3, no material property (E, ν) information is passed to the iFEM, since just strain-displacement relationships are employed in the method.

The method described in Section 3 exploits the measured strain deviation due to damage occurrence. Since the component is reasonably assumed to be undamaged at the beginning of its service life, the element connectivity within the M_{iFEM} presents no hint of crack presence and, in fact, the iFEM model of the structure is always assumed to be in a healthy condition, thus possibly highlighting the non-compatibility of the measured strain (here simulated with direct FEM as in Figure 8 and Figure 9), corresponding to damaged condition.

Two different sensor grids, providing a measure on the top and bottom surfaces for each sensor position (x_{in}), are employed as input to the iFEM $(\boldsymbol{\varepsilon_{in}})$, the first one (ID1) is a strain rosette for each inverse element (Figure 11a), while the second one (ID2) is a strain rosette in a limited number of inverse elements (Figure 11b). In fact, in reality, one is not able to provide each element with a strain measure for economical and practical issues. The results indicate that limiting the sensor number does not hamper the method applicability. However, the sensor grid must be defined taking the load configuration and damage configuration into account in order to guarantee enough damage sensitivity and identification accuracy. Specifically, in a real application, the sensor network will be optimised based on the type of load the structure is undergoing, the structure geometry, as well as the desired accuracy and precision of the feature extraction, possibly allowing a unidirectional strain measure at sensor positions, thus enabling the adoption of distributed strain sensing technologies, e.g. based on fiber optic sensors.

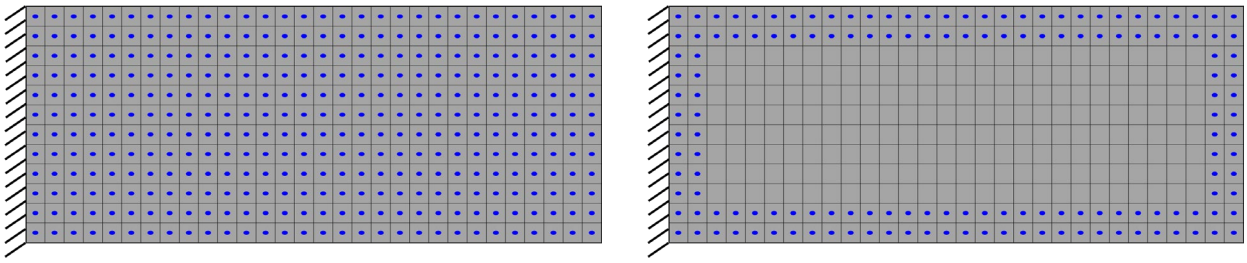

(a) (b)

Figure 11: Different sensors grid; (a) Sensors grid ID1; (b) Sensors grid ID2

The same test sensor grid ($\boldsymbol{\varepsilon_t}$) is employed for anomaly index computation, both for the analysis with the sensor grid ID1 and ID2. The test sensors consist again of strain rosettes located as shown in Figure 12. The regions close to the clamp and the applied load are not considered for brevity and to avoid possible errors due to the vicinity of the edges, without loss of validity. However, additional tests not reported here for brevity and performed considering the sensor positions near the edges, confirmed the presence and the position of the crack can be identified with sufficient accuracy. It has to be noticed that this test sensor grid is used in order to verify feature sensitivity distributions all over the component surface, simply assuming a sensor is present in all the iFEM mesh elements. In a real application one will only add sensors in regions either more prone to fatigue damage initiation or more critical for inspection, or even just consider $\boldsymbol{x_t} = \boldsymbol{x_{in}}$.

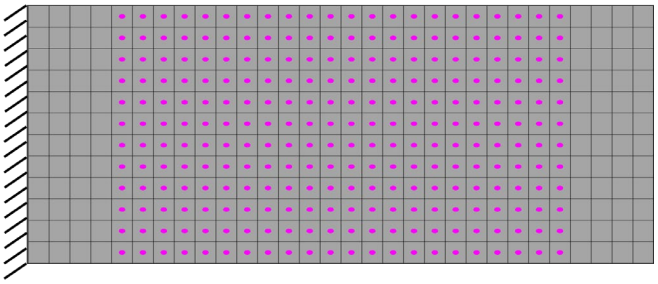

Figure 12: Test sensors grid

5. Results

The results of the numerical simulations of the clamped plate described in Section 4 subjected to different loading conditions are presented in this section. Hereafter, the focus is on demonstrating the possibility of creating a load-independent feature baseline, by testing the algorithm behaviour when some of the hypotheses made in Section 3.2 are not respected. In Section 5.1 and 5.1.1 the algorithm performance is tested when the number of inverse elements for mesh discretisation is limited. Specifically, Section 5.1.1 provides a comparison for two different iFEM discretisations: a coarse and a fine mesh. The method is then tested in Section 5.2 when the hypotesis of having a one-to-one sensorisation (i.e. each inverse element instrumented with a strain rosette) is no longer met. Finally, the method is tested in Section 5.3 and Section 5.4 with different sizes, locations, numbers and orientations of the crack damages, aiming at demonstrating the generality of the method.

5.1 Plate under different loading conditions with a strain rosette for each mesh element

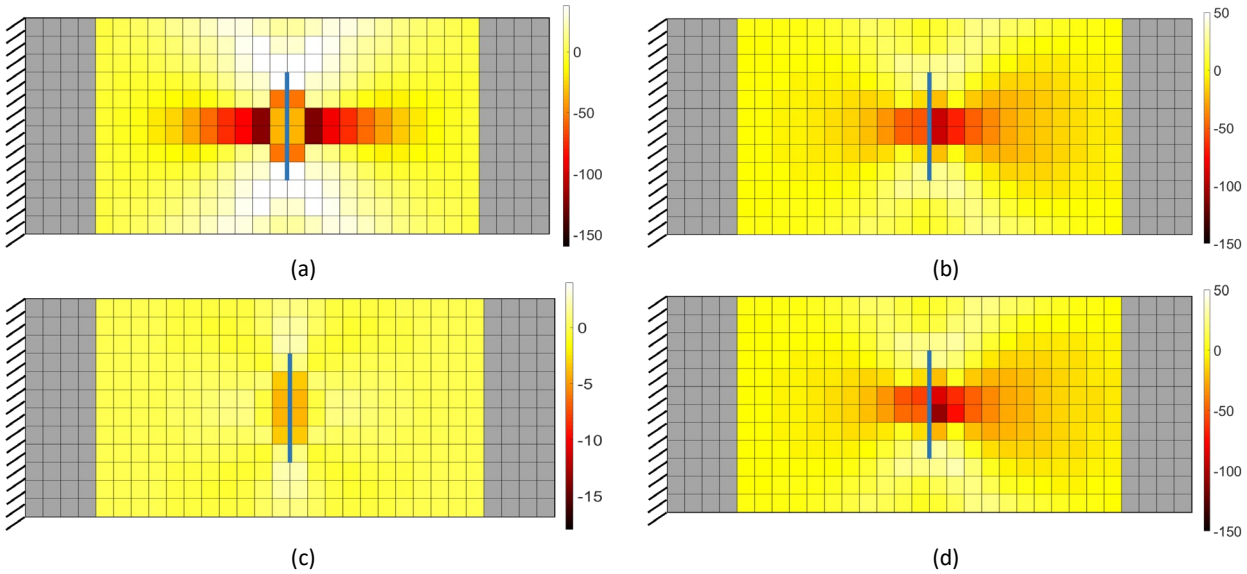

Figure 13: Anomaly index computed under different load conditions based on sensor input ID1; (a) load condition 1; (b) load condition 2; (c) load condition 3; (d) load condition 4. Crack is always located in the center of the plate, with orientation as in Figure 7a (blue line).

	Anomaly Index magnitude of the healthy structure in % (max)	**Anomaly Index magnitude of the cracked structure in % (max)**
Plate under loading condition 1	0.14	123.08
Plate under loading condition 2	0.39	92.08
Plate under loading condition 3	0.13	3.92
Plate under loading condition 4	0.39	106.48

Table 2: Maximum magnitude of the anomaly index in a healthy and damaged condition for different loading conditions

The damage identification results for the general case when a rosette strain gauge is located at each mesh node, corresponding to sensors grid ID1 in Figure 11a, are shown here. Subplots in Figure 13 present the anomaly index results, calculated for each mesh element, under the different loading conditions highlighted in Section 4.1.

The peak value (in magnitude) of the anomaly index is also reported in Table 2, comparing the two conditions of healthy and damaged structure, again separately for each load configuration. The baseline error, or the envelope of the anomaly index for the undamaged case, remains close to zero, thus verifying the capability of the iFEM to reconstruct the strain field and to adjust the baseline as a function of different input load configurations. The maximum value in magnitude of the anomaly index presents a high damage sensitivity, reflected in a significant difference between the damaged and healthy conditions. In particular, if the structure is undamaged, the corresponding maximum value (in magnitude) of the strain field reconstruction error is close to zero (e.g. 0.14% for loading condition 1); on the contrary, if the structure is damaged, it is different from zero (e.g. 123% for loading condition 1). The former error is related to a different mesh discretisation of the iFEM model with respect to the direct FEM simulation in Figure 8, as well as due to the computational procedure of the strain field involving the extrapolation of the results, starting from the values computed at the Gauss Points, by means of functions which can lead to differences between the direct and inverse FEM solution. The latter is due to the iFEM impossibility to reconstruct a displacement field compatible with the test strain measures in the presence of a crack, since the iFEM input model mesh presents no crack.

Furthermore, the closer the position for the anomaly index computation is to the crack edge, the lower the anomaly index is, indicating the anomaly index distribution can also be exploited for the damage localisation. For the loading condition 1, an unexpected sensitivity decrease can be noticed in correspondence of the crack edge (Figure 8a). However, this is not a deficiency of the method but is related to approximations of the direct FEM solution that is used here for simulating sensor measures.

However, the anomaly index sensitivity to damage remains dependent on the load configuration. In fact, if in the case of the loading condition 1,2 and 4 a relatively high sensitivity is found also at a significant distance from the damage, less sensitivity is shown in Figure 13c for the loading condition 3 (i.e. torque). This is related to a limited difference of the shear deformations (γ_{xy}) between the healthy and damage states, as well as to a more local effect of the crack over the strain field, as highlighted in Figure 8c. This fact traduces in Table 2 in a limited difference in the magnitude of the Anomaly indices calculated for the damaged and healthy conditions for the load case 3.

5.1.1 Influence of the iFEM mesh

It is known that the mesh size can influence the results of the iFEM analysis [54]. However, a compromise between the precision and the computational effort is necessary in view of a real-time implementation. For this reason, before assessing the performance of the approach with a limited number of sensors (Section 5.2), the influence of the iFEM model mesh size on the anomaly index results has been checked. For brevity, only the results of the simulations with the loading condition 1 are presented here, even though the same considerations can be easily extended also to the other cases.

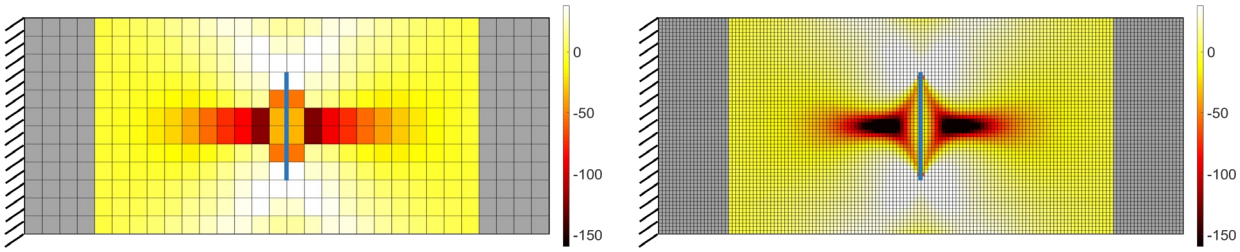

(a) (b)

Figure 14: Anomaly index with different iFEM mesh sizes; (a) Coarse mesh (360 EF); (b) Fine mesh (9000 EF)

	Anomaly Index magnitude of the healthy structure in % (max)	**Anomaly Index magnitude of the cracked structure in % (max)**
Plate under loading condition 1 (MESH coarse)	0.14	123.08
Plate under loading condition 1 (MESH fine)	0.01	282.81

Table 3: Maximum magnitude of the anomaly index in a healthy and damaged condition for different mesh sizes

A second finer mesh is considered (Figure 14b), in which the structure presents the same discretisation of the reference FEM model employed for the strain simulation and composed by 9000 inverse elements with a dimension of 1 mm. iFEM simulations results are compared to those obtained before based on a coarser mesh (Figure 14a) composed by 360 inverse elements with a dimension of 5 mm. As in the previous section, a strain rosette is considered at each mesh element and the simulated strains in Figure 8 are used as virtual measures.

The anomaly index distribution and magnitude appear to be dependent on the mesh size. Referring to Figure 14, a fine mesh generates a more precise strain field reconstruction with respect to a coarse mesh. This

reasonably results in a more precise distribution and higher peak magnitudes of the anomaly index. However, a finer mesh requires a greater number of sensors and a greater computational effort. Thus, a trade-off is needed for a realistic implementation.

A comparison of the maximum anomaly index magnitude obtained with two mesh resolutions is shown in Table 3 for the healthy and damaged state. On one hand, the maximum value in magnitude of the anomaly index computed with a fine mesh in a healthy condition drops down to 0.01%, indicating that most of the baseline error found in Section 5.1 is caused by iFEM mesh discretisation. On the other hand, it rises to a value of about 283% in the presence of the crack, indicating that a coarse mesh averages the anomaly index magnitude within each element area. In general, the finer the mesh, the greater the sensitivity of the anomaly index to the presence of a damage will be. However, damage can be detected and localised with sufficient (though different) precision with both mesh discretisations.

5.2 Plate under different loading conditions with a strain rosette on selected elements

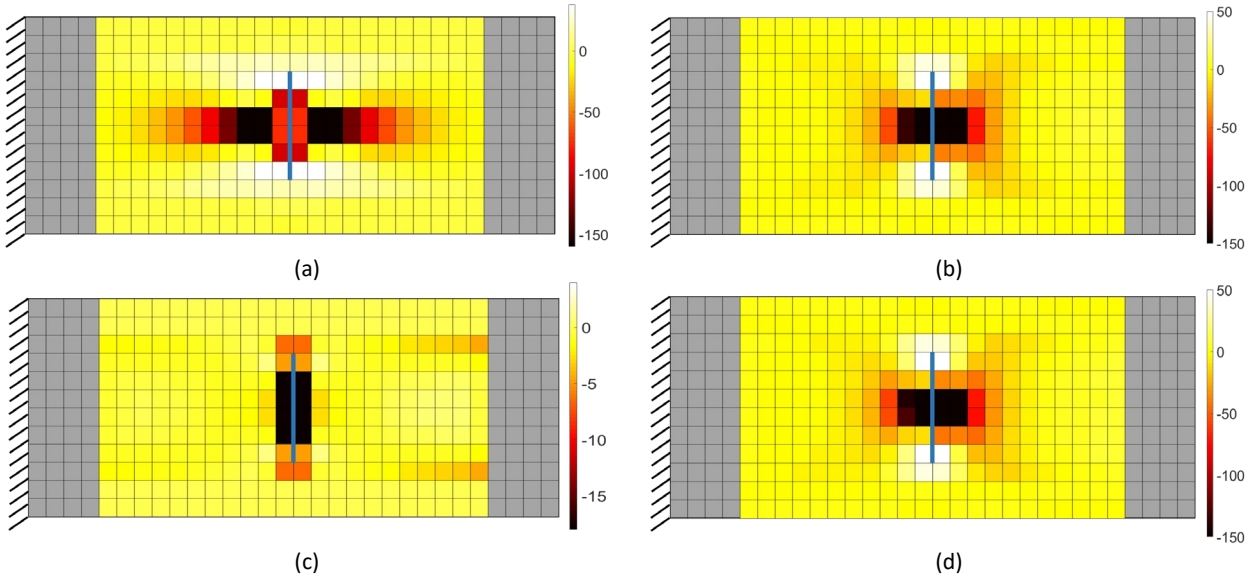

Figure 15: Anomaly index computed under different load conditions based on sensor input ID2; (a) load condition 1; (b) load condition 2; (c) load condition 3; (d) load condition 4. Crack is always located in the center of the plate, with orientation as in Figure 7a (blue line).

	Anomaly Index magnitude of the healthy structure in % (max)	**Anomaly Index magnitude of the cracked structure in % (max)**
Plate under loading condition 1	0.99	203.44
Plate under loading condition 2	3.10	352.99
Plate under loading condition 3	4.63	28.90
Plate under loading condition 4	5.78	394.40

Table 4: Maximum magnitude of the anomaly index in a healthy and damaged condition for different loading conditions

The anomaly index behaviour when the strain field is reconstructed by the iFEM including sensors only at some mesh elements is now investigated. In particular, input measures correspond to sensor network ID2 (Figure 11b). Again, subplots in Figure 15 present the anomaly index results, calculated for each mesh element, under the different loading conditions highlighted in Section 4.1. The same colour scale is used as in Figure 13, in order to facilitate the understanding of the effect of a different sensor layout. The peak value

(in magnitude) of the anomaly index is also reported in Table 4, for the healthy and damaged conditions and separately for each load configuration.

First, referring to results in Figure 15, the detection and localisation of a damage can be accomplished independently from the sensors grid considered, however, provided a correct reconstruction of the displacement field in case of undamaged structure is still guaranteed by the iFEM algorithm. Though a limited number of sensors is used with respect to the previous analyses, the highest sensitivity of the anomaly index is still in correspondence with the crack.

Second, Table 4 clearly confirms the baseline adaptability to different loading conditions. Some error is introduced in the iFEM strain field reconstruction if a limited number of sensors is adopted, thus provoking a wider baseline envelope for the anomaly index, which is reflected in a higher magnitude of the anomaly index for the undamaged state if compared to Table 2. However, the maximum magnitude of the anomaly index remains close to zero for the undamaged structure and its maximum magnitude with damage is considerably different from that of a healthy structure.

Few more comments are worth making to understand the effect of the sensor grid as input to the iFEM over the damage identification. Comparing Table 2 with Table 4 it can be easily noticed that the values of the anomaly index in the two analyses are different. In particular, it appears that the sensitivity with the sensor grid ID2 is higher with respect to the condition in which each element is instrumented with a sensor. If all the elements are instrumented with a strain rosette (sensor network ID1), the strain measures in the vicinity of the damage contain information about the damage itself and the anomaly index sensitivity is only related to a mismatch between the elements connectivity in the iFEM mesh and the real structure, here corresponding to the direct FEM mesh, which includes the crack. On the other hand, when only a few elements are instrumented with a sensor and these elements are far from the crack location (sensor network ID2), the input strain pattern used by iFEM to reconstruct the displacement and strain fields is influenced by the damage to a lower degree. This is reflected in a higher mismatch between the $\boldsymbol{\varepsilon_{iFEM}}$ and $\boldsymbol{\varepsilon_t}$ used for the anomaly index evaluation, which is related to higher non-compatibility of $\boldsymbol{U}$ with $\boldsymbol{\varepsilon_t}$ due to the absence of information about the damage in the input measures, $\boldsymbol{\varepsilon_{in}}$. In fact, the iFEM reconstructs a strain field $\boldsymbol{\varepsilon_{iFEM}}$ (compatible with $\boldsymbol{U}$) significantly different from the measures at test locations ($\boldsymbol{\varepsilon_t}$), thus making sensitivity higher for sensor network ID2 with respect to ID1. This analysis points out that the anomaly index magnitude depends on the sensors grid employed for the iFEM strain field reconstruction, and this has to be taken into consideration during sensor network optimisation.

5.3 Plate under different loading conditions with a strain rosette on selected elements and a crack oriented at 45 degrees

The damage identification results for the plate in Figure 7b with a crack oriented at 45 degrees are reported hereon to investigate the method robustness with respect to different damage parameters and locations. Subplots of Figure 16 show the anomaly index results at each test sensor position under the different loading conditions described in Section 4.1. In particular, for the sake of brevity, just the results obtained with the input sensors grid ID2 are reported, however representing the most challenging sensors grid between the two considered in Figure 11.

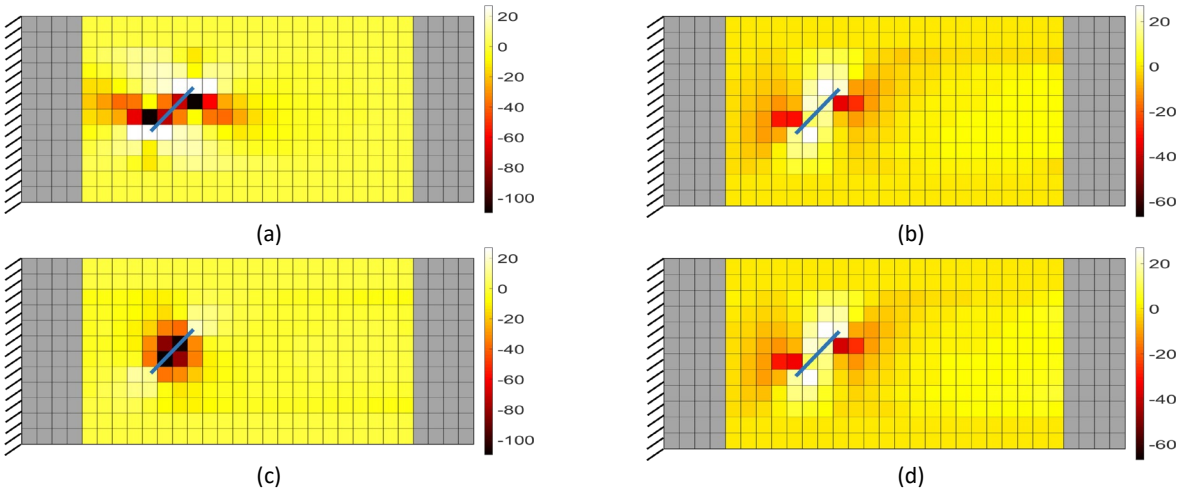

Figure 16: Anomaly index computed under different load conditions based on sensor input ID2; (a) load condition 1; (b) load condition 2; (c) load condition 3; (d) load condition 4. A 20 mm crack oriented at 45 degrees is located at 50 mm from the clamp as shown in blue.

	Anomaly Index magnitude of the healthy structure in % (max)	**Anomaly Index magnitude of the cracked structure in % (max)**
Plate under loading condition 1	0.99	183.29
Plate under loading condition 2	3.10	34.83
Plate under loading condition 3	4.63	112.05
Plate under loading condition 4	5.78	38.20

Table 5: Maximum magnitude of the anomaly index in a healthy and damaged condition for different loading conditions

The peak value (in magnitude) of the anomaly index is once again reported in Table 5, separately for each load case, for the healthy and damaged scenarios. The maximum value presents a high damage sensitivity, reflected in a significant difference in the damaged condition with respect to the envelop of the healthy structure baseline. Despite the varied damage position, orientation and size, very high values of the index are found in correspondence of the defect (e.g. about 183% for the loading condition 1) for each of the cases shown in Table 5. Furthermore, as for the previous case studies with the crack oriented as in Figure 7a, the distribution of the index values within the plate confirms the appealing of the method also for damage localisation and the generality of the damage identification procedure with respect to the damage size, position and orientation. Indeed, the minimum of the index is always found in correspondence of the defect independently from the loads acting on the structure. However, the anomaly index sensitivity remains dependent on the load shape. In fact, the damage sensitivity is different according to the different strain distributions within the structure due to the different loading conditions, moving from a larger sensitivity for loading conditions 1 and 3 to a lower, but significant, sensitivity for loading conditions 2 and 4.

5.4 Plate under different loading conditions with a strain rosette on selected elements and two cracks of different sizes and positions

The damage identification outcomes for the damaged scenarios in Figure 7c and Figure 7d are presented hereafter to demonstrate the method robustness in presence of multiple damages, with different sizes and positions. Subplots of Figure 17 show the anomaly index results at each test sensor position under the different loading conditions described in Section 4.1 and for different crack sizes and positions. In particular,

only the results obtained with the input sensors grid ID2 are described for brevity, although the outcomes are easily extendable to the input sensors grid ID1.

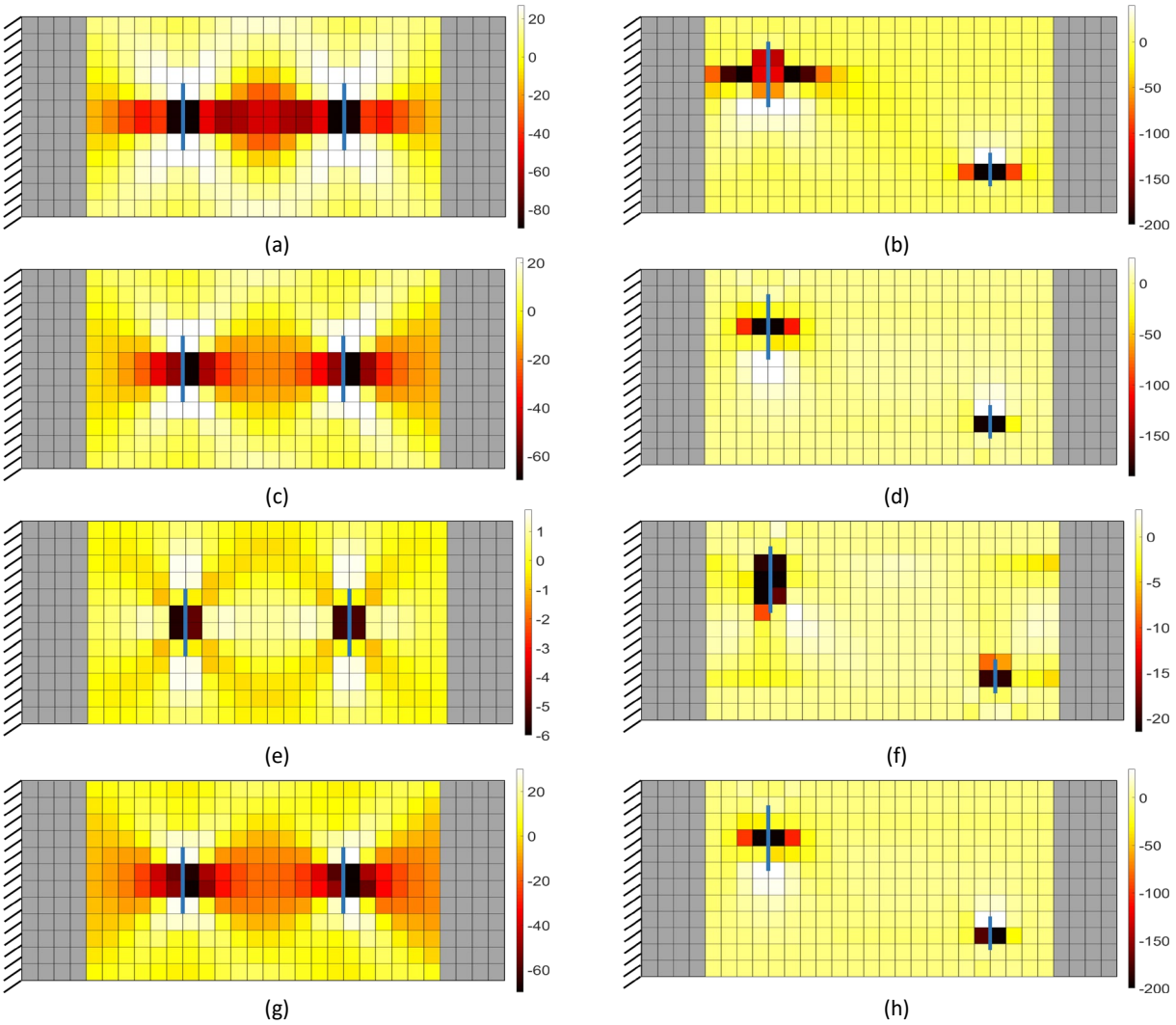

Figure 17: Anomaly index computed under different load conditions based on sensor input ID2 and the two cracks positioned as in Figure 7c and Figure 7d; (a) load condition 1 and the two cracks as in Figure 7c; (b) load condition 1 and the two cracks as in Figure 7d; (c) load condition 2 and the two cracks as in Figure 7c; (d) load condition 2 and the two cracks as in Figure 7d; ; (e) load condition 3 and the two cracks as in Figure 7c; (f) load condition 3 and the two cracks as in Figure 7d; (g) load condition 4 and the two cracks as in Figure 7c; (h) load condition 4 and the two cracks as in Figure 7d. The two cracks are shown in blue.

	Two cracks of the same dimension positioned close to each other		**Two cracks of different dimension positioned far from each other**	
	Anomaly Index of the left crack [%] (max)	**Anomaly Index of the right crack [%] (max)**	**Anomaly Index of the left crack [%] (max)**	**Anomaly Index of the right crack [%] (max)**
Plate under loading condition 1	96.84	94.70	463.75	296.58
Plate under loading condition 2	68.71	80.12	887.15	245.14
Plate under loading condition 3	5.69	5.38	31.05	20.15
Plate under loading condition 4	74.32	94.03	831.47	217.84

Table 6: Maximum magnitude of the anomaly index in a damaged condition with two cracks of different sizes and positions, reported separately for the left and the right crack.

The anomaly index peak values for the two damaged scenarios are reported in Table 6 separately for each damaged condition and crack positions. Despite the simultaneous presence of multiple damages, a high damage sensitivity can be noticed by looking at the peak values of the anomaly index in the damaged state (e.g. about 97 % for the loading condition 1), while the peak values remain close to zero for the undamaged condition (e.g. about 0.99 % for the loading condition 1). Less sensitivity to damage is found for the loading condition 3 (i.e. torque), reflected in a lower difference between the peak values for the healthy and damaged scenarios, although sufficient for robust damage identification.

It has to be noticed that the anomaly index magnitude varies as a function of the crack length, as justified by a different strain field perturbation. In particular, almost the same value (Table 6) is found in correspondence of the two crack positions in Figure 7c, while a different peak value is found in correspondence of the two defects when considering a damaged scenario like in Figure 7d. Indeed, referring to the Table 6, one can notice that a greater value of the index is observed for the $20\,mm$ long crack, while a smaller, though significant, anomaly indication is found for the $10\,mm$ long crack.

Finally, very good localization is achieved also in the case of multiple damages, when the two defects do not influence each other, as for the damaged scenario in Figure 7d. On the contrary, if the two defects are close to each other, a more spread area of influence can be noticed (second column in Figure 17) due to the interaction between the two defects causing a mutual influence in the strain field. However, the peak values in magnitude of the anomaly index are correctly located in the areas closest to the cracks, confirming that the presence of multiple defects does not hamper the ability of the method to correctly localize the damage.

Conclusions

In this work, a new feature for anomaly identification is derived by inverse Finite Element Method. The iFEM ability to reconstruct the structure deformations on the basis of input strain measures at discrete positions without any a priori training and without knowledge regarding the acting loads is adopted to define a load-adaptive baseline, which can be easily implemented in damage identification scenarios.

An anomaly index is defined as the percentage difference between an equivalent strain read at a test sensor position and the one reconstructed by the iFEM algorithm at the same position. Ideally, if a proper mesh discretisation is adopted, if a sufficient number of input strain sensors is considered and if the sensor noise is neglected, the iFEM will enable maintaining a constant zero valued pattern of anomaly indices for the healthy structure independently from the load or combination of loads acting on the structure at the time instant considered. Deviation from the simplifying hypothesis will cause a small, but quantifiable, increase of the baseline domain. On the contrary, in a damaged structure, the anomaly index will largely differ from zero at some test positions in the vicinity of the defect.

The validity of the proposed method is confirmed by the results. A significant sensitivity is noticed comparing the healthy and damaged condition of a clamped plate subject to different load configurations in a virtual environment, proving the method suitability for anomaly detection in presence of crack damages with different positions, number, orientations and sizes. The load-adaptivity of the baseline is also verified for different mesh discretisation, being the anomaly index peak values close to zero for the healthy cases independently from the applied load, with values approaching zeros for finer iFEM meshes. Furthermore, little loss of precision for damage localisation upon varying the load condition is shown. Indeed, the peak value of the anomaly index is always found in the vicinity of the crack edge.

Concerning the number of required strain measures, this includes (i) sensors as input to the iFEM for strain field reconstruction and (ii) sensors at test positions for damage identification, the latter being potentially included in the former. In this work the method applicability with two sensor networks as input to the iFEM, the first including a strain rosette at each mesh element, the second limiting sensors at the plate perimeter is positively demonstrated. In particular, strain rosettes are used to measure three strain tensor components, for strain field reconstruction under different load configurations allowing to pose no limit in the type of load acting on the structure, given a sufficient number of strain rosettes were used as input to the iFEM.

Though existing strain measure technologies, e.g. based on fiber optics, facilitate the acquisition of a dense sensor network, in realistic structures the number of measures has to be limited, possibly allowing the measure of a single strain tensor component. Though not reported here being matter of present and future research by the authors, the method remains valid if just a mono-axial strain component is measured, however implying a loss of generality concerning the iFEM ability to reconstruct the strain field of the structure independently of the type of load. This is however compatible with most of the structural components which possess preferential load transfer capabilities and has to be taken into account during sensor network design. Furthermore, future research by the authors will be devoted to the experimental validation of the method, thus exploring the effect of noise and modelling uncertainties on the structural diagnosis.

Appendix A

The transformation matrix ($\boldsymbol{T}^i$) and the local nodal coordinates of the element introduced in Section 2.1 are derived hereafter.

By calling:

$$\boldsymbol{X}_q = \begin{Bmatrix} X_q \\ Y_q \\ Z_q \end{Bmatrix} (q = 1,2,3,4) \tag{A.1}$$

the global coordinates of the q^{th} element node, the three unitary vectors $\boldsymbol{l}, \boldsymbol{p}, \boldsymbol{n}$ defining the local reference system are calculated as:

$$\begin{aligned} \boldsymbol{n} &= \frac{\boldsymbol{X_{31}} \wedge \boldsymbol{X_{42}}}{\left|\left|\boldsymbol{X_{31}} \wedge \boldsymbol{X_{42}}\right|\right|} \\ \boldsymbol{p} &= \frac{\boldsymbol{X_{31}} + \boldsymbol{X_{42}}}{\left|\left|\boldsymbol{X_{31}} + \boldsymbol{X_{42}}\right|\right|} \\ \boldsymbol{l} &= \boldsymbol{p} \wedge \boldsymbol{n} \end{aligned} \tag{A.2}$$

where

$$\boldsymbol{X_{31}} = \boldsymbol{X}_3 - \boldsymbol{X}_1$$

is the diagonal vector pointing from node 1 to 3, while

$$\boldsymbol{X_{42}} = \boldsymbol{X}_4 - \boldsymbol{X}_2$$

is the one pointing from node 2 to 4.

Exploiting Eq. (A.2), the transformation matrix of the nodal d.o.f. of the i^{th} element from local to global coordinate system is, thus, defined as:

$$\boldsymbol{T}^i = \begin{bmatrix} \boldsymbol{T} & \boldsymbol{0} & \boldsymbol{0} & \boldsymbol{0} & \boldsymbol{0} & \boldsymbol{0} & \boldsymbol{0} & \boldsymbol{0} \\ \boldsymbol{0} & \boldsymbol{T} & \boldsymbol{0} & \boldsymbol{0} & \boldsymbol{0} & \boldsymbol{0} & \boldsymbol{0} & \boldsymbol{0} \\ \boldsymbol{0} & \boldsymbol{0} & \boldsymbol{T} & \boldsymbol{0} & \boldsymbol{0} & \boldsymbol{0} & \boldsymbol{0} & \boldsymbol{0} \\ \boldsymbol{0} & \boldsymbol{0} & \boldsymbol{0} & \boldsymbol{T} & \boldsymbol{0} & \boldsymbol{0} & \boldsymbol{0} & \boldsymbol{0} \\ \boldsymbol{0} & \boldsymbol{0} & \boldsymbol{0} & \boldsymbol{0} & \boldsymbol{T} & \boldsymbol{0} & \boldsymbol{0} & \boldsymbol{0} \\ \boldsymbol{0} & \boldsymbol{0} & \boldsymbol{0} & \boldsymbol{0} & \boldsymbol{0} & \boldsymbol{T} & \boldsymbol{0} & \boldsymbol{0} \\ \boldsymbol{0} & \boldsymbol{0} & \boldsymbol{0} & \boldsymbol{0} & \boldsymbol{0} & \boldsymbol{0} & \boldsymbol{T} & \boldsymbol{0} \\ \boldsymbol{0} & \boldsymbol{0} & \boldsymbol{0} & \boldsymbol{0} & \boldsymbol{0} & \boldsymbol{0} & \boldsymbol{0} & \boldsymbol{T} \end{bmatrix} \tag{A.3}$$

with

$$\boldsymbol{T} = [\boldsymbol{l}^{\boldsymbol{T}}\ \boldsymbol{p}^{\boldsymbol{T}}\ \boldsymbol{n}^{\boldsymbol{T}}]^{\boldsymbol{T}}$$

the transformation matrix from local to global coordinate system. Note that $\boldsymbol{T}$ is a 3x3 matrix (3 displacements/rotations for each node), while $\boldsymbol{T}^i$ is a 24x24 matrix, since the iQS4 element has 24 d.o.f.: 6 (i.e. 3 displacements and 3 rotations) for each node.

Then, in order to compute the local nodal coordinates of the i^{th} element with respect to a reference system centered in the element centroid (Figure 1), the global coordinates $\boldsymbol{C}$ of the centroid needs to be calculated as:

$$\boldsymbol{C} = \frac{\sum_{\alpha=1}^{4} \boldsymbol{c}_\alpha d_\alpha}{\sum_{\alpha=1}^{4} d_\alpha} \tag{A.4}$$

where d_α is the edge length and $\boldsymbol{c}_\alpha$ the edge mid-point defined as:

$$\left.\begin{aligned} d_\alpha &= \left|\left|\boldsymbol{X}_\beta - \boldsymbol{X}_\alpha\right|\right| \\ \boldsymbol{c}_\alpha &= \frac{\boldsymbol{X}_\beta + \boldsymbol{X}_\alpha}{2} \end{aligned}\right\} (\alpha = 1,2,3,4; \beta = 2,3,4,1) \tag{A.5}$$

Once the element centroid is defined as in Eq. (A.4), the local nodal coordinates of the element are finally calculated as:

$$\left.\begin{aligned} x_q &= (\boldsymbol{X}_q - \boldsymbol{C}) \cdot \boldsymbol{l} \\ y_q &= (\boldsymbol{X}_q - \boldsymbol{C}) \cdot \boldsymbol{p} \end{aligned}\right\} (q = 1,2,3,4) \tag{A.6}$$

Appendix B

The explicit form of the shape functions used for the definition of the iQS4 element are:

$$
\begin{aligned}
N_1 &= \frac{(1-s)(1-t)}{4} \\
N_2 &= \frac{(1+s)(1-t)}{4} \\
N_3 &= \frac{(1+s)(1+t)}{4} \\
N_4 &= \frac{(1-s)(1+t)}{4} \\
L_1 &= y_{14}N_8 - y_{21}N_5 \\
L_2 &= y_{21}N_5 - y_{32}N_6 \\
L_3 &= y_{32}N_6 - y_{43}N_7 \\
L_4 &= y_{43}N_7 - y_{14}N_8 \\
M_1 &= x_{41}N_8 - x_{12}N_5 \\
M_2 &= x_{12}N_5 - x_{23}N_6 \\
M_3 &= x_{23}N_6 - x_{34}N_7 \\
M_4 &= x_{34}N_7 - x_{41}N_8
\end{aligned}
\tag{B.1}
$$

with $x_{\alpha\beta}$ and $y_{\alpha\beta}$

$$
\left.\begin{aligned} x_{\alpha\beta} &= x_\alpha - x_\beta \\ y_{\alpha\beta} &= y_\alpha - y_\beta \end{aligned}\right\} (\alpha = 1,2,3,4;\ \beta = 1,2,3,4) \tag{B.2}
$$

while

$$
\begin{aligned}
N_5 &= \frac{(1-s^2)(1-t)}{16} \\
N_6 &= \frac{(1+s)(1-t^2)}{16} \\
N_7 &= \frac{(1-s^2)(1+t)}{16} \\
N_8 &= \frac{(1-s)(1-t^2)}{16}
\end{aligned}
\tag{B.3}
$$

By exploiting these shape functions, the matrices $\boldsymbol{B^m}, \boldsymbol{B^b}, \boldsymbol{B^s}$ can be obtained and their explicit form is:

$$
\begin{aligned}
\boldsymbol{B^m} &= [\boldsymbol{B_1^m}\ \boldsymbol{B_2^m}\ \boldsymbol{B_3^m}\ \boldsymbol{B_4^m}] \\
\boldsymbol{B^b} &= \left[\boldsymbol{B_1^b}\ \boldsymbol{B_2^b}\ \boldsymbol{B_3^b}\ \boldsymbol{B_4^b}\right] \\
\boldsymbol{B^s} &= [\boldsymbol{B_1^s}\ \boldsymbol{B_2^s}\ \boldsymbol{B_3^s}\ \boldsymbol{B_4^s}]
\end{aligned}
\tag{B.4}
$$

in which:

$$\left.\begin{aligned}
\boldsymbol{B}_q^{\boldsymbol{m}} &= \begin{bmatrix} \frac{\partial N_q}{\partial x} & 0 & 0 & 0 & 0 & \frac{\partial L_q}{\partial x} \\ 0 & \frac{\partial N_q}{\partial y} & 0 & 0 & 0 & \frac{\partial M_q}{\partial y} \\ \frac{\partial N_q}{\partial y} & \frac{\partial N_q}{\partial x} & 0 & 0 & 0 & \frac{\partial L_q}{\partial y} + \frac{\partial M_q}{\partial x} \end{bmatrix} \\
\boldsymbol{B}_q^{\boldsymbol{b}} &= \begin{bmatrix} 0 & 0 & 0 & 0 & \frac{\partial N_q}{\partial x} & 0 \\ 0 & 0 & 0 & -\frac{\partial N_q}{\partial y} & 0 & 0 \\ 0 & 0 & 0 & -\frac{\partial N_q}{\partial x} & \frac{\partial N_q}{\partial y} & 0 \end{bmatrix} \\
\boldsymbol{B}_q^{\boldsymbol{s}} &= \begin{bmatrix} 0 & 0 & \frac{\partial N_q}{\partial x} & -\frac{\partial L_q}{\partial x} & -\frac{\partial M_q}{\partial x} + N_q & 0 \\ 0 & 0 & \frac{\partial N_q}{\partial y} & -\frac{\partial L_q}{\partial y} - N_q & -\frac{\partial M_q}{\partial y} & 0 \end{bmatrix}
\end{aligned}\right\} (q = 1, 2, 3, 4) \quad \text{(B.5)}$$

Appendix C

The Jacobian operator is required to compute the partial derivatives of the shape functions with respect to x and y coordinates. It is computed as:

$$\boldsymbol{J} = \frac{\partial(x, y)}{\partial(s, t)} = \begin{bmatrix} \frac{\partial x}{\partial s} & \frac{\partial y}{\partial s} \\ \frac{\partial x}{\partial t} & \frac{\partial y}{\partial t} \end{bmatrix} \quad \text{(C.1)}$$

Where the partial derivatives of the x and y coordinate with respect to s and t are equal to:

$$\begin{aligned}
\frac{\partial x}{\partial s} &= \sum_{q=1}^{4} \frac{\partial N_q}{\partial s}\, x_q \\
\frac{\partial x}{\partial t} &= \sum_{q=1}^{4} \frac{\partial N_q}{\partial t}\, x_q \\
\frac{\partial y}{\partial s} &= \sum_{q=1}^{4} \frac{\partial N_q}{\partial s}\, y_q \\
\frac{\partial y}{\partial t} &= \sum_{q=1}^{4} \frac{\partial N_q}{\partial t}\, y_q
\end{aligned} \quad \text{(C.2)}$$

Finally, the partial derivatives of the generic $(\cdot)$ shape function can be written in matrix form as:

$$\begin{bmatrix} \frac{\partial(\cdot)}{\partial x} \\ \frac{\partial(\cdot)}{\partial y} \end{bmatrix} = \begin{bmatrix} \frac{\partial s}{\partial x} & \frac{\partial t}{\partial x} \\ \frac{\partial s}{\partial y} & \frac{\partial t}{\partial y} \end{bmatrix} \begin{bmatrix} \frac{\partial(\cdot)}{\partial s} \\ \frac{\partial(\cdot)}{\partial t} \end{bmatrix} = \frac{\partial(s, t)}{\partial(x, y)} \begin{bmatrix} \frac{\partial(\cdot)}{\partial s} \\ \frac{\partial(\cdot)}{\partial t} \end{bmatrix} = \boldsymbol{J}^{-1} \begin{bmatrix} \frac{\partial(\cdot)}{\partial s} \\ \frac{\partial(\cdot)}{\partial t} \end{bmatrix} \quad \text{(C.3)}$$

Where $\boldsymbol{J}^{-1}$ is the inverse of the Jacobian matrix.

Nomenclature

$(\cdot^{\boldsymbol{\varepsilon}})$	Measured strain field component
$\big(\cdot\,(\boldsymbol{u})\big)$	Numerical formulation of the strain field component
$\boldsymbol{e}_{i,j}$	j^{th} membrane deformation component associated to the reference plane of the i^{th} element
$\boldsymbol{k}_{i,j}$	j^{th} bending deformation component associated to the reference plane of the i^{th} element
$\boldsymbol{g}_{i,j}$	j^{th} transverse shear deformation component associated to the reference plane of the i^{th} element
Φ	Weighted least-squares functional
w_m, w_b, w_s	Weight of the functional associated to the membrane, bending and shear deformation respectively
$\boldsymbol{u}$	Vector of nodal degrees of freedom in local coordinates
$\boldsymbol{B^m}, \boldsymbol{B^b}, \boldsymbol{B^s}$	Matrix of the shape function derivatives associated to the membrane, bending and shear behaviour respectively
$\boldsymbol{x}_j$	j^{th} sensor position within an inverse element
ε, γ	Strain tensor component
x, y, z	Local coordinate axes
X, Y, Z	Global coordinate axes
h	Semi-thickness of the element
$\cdot^+$	Top surface component
$\cdot^-$	Bottom surface component
$\boldsymbol{U}$	Vector of nodal degrees of freedom in global coordinates
$\boldsymbol{K}$	Global left-hand side matrix
$\boldsymbol{F}$	Global right-hand side vector
Ξ	Global parameter function of the values of the measured strains
$\boldsymbol{\varepsilon_{in}}$	Measured input strain values
$\boldsymbol{\varepsilon_{iFEM}}$	Reconstructed strain field
M_{iFEM}	iFEM-based model for real-time calculation of the strain field $\boldsymbol{\varepsilon_{iFEM}}$ as a function of $\boldsymbol{\varepsilon_{in}}$
Ω	Structural domain
A	Mid-plane area
$\boldsymbol{x_{in}}$	Input sensor positions
n_{in}	Number of input strain sensor positions
$n_{st,in}$	Number of input strain tensor components measured at $\boldsymbol{x_{in}}$
$\boldsymbol{\varepsilon_t}$	Test strain measures
$\boldsymbol{x_t}$	Test sensor positions
n_t	Number of test strain sensor positions
$n_{st,t}$	Number of test strain tensor components measured at $\boldsymbol{x_t}$
ε_{eq}	Equivalent strain proportional to the second invariant of the deviatoric strain tensor
i	Anomaly index
l	Load
$\boldsymbol{T}$	Transformation matrix from local to global coordinate system
L, M, N	Shape functions
s, t	Isoparametric coordinates
u, v	Membrane displacements
w	Transverse displacements
θ_x, θ_y	Bending rotations
u_x, u_y	In-plane displacements
u_z	Deflection across the uniform shell thickness
$\boldsymbol{k}^i$	Local matrix of the i^{th} element independent of the measured strain values

$\boldsymbol{f}^i$	Local vector of the i^{th} element function of both the number and the values of the measured strains
$\boldsymbol{\xi^i}$	Local parameter of the i^{th} element function of the measured strains
$\boldsymbol{E_i}$	Extraction matrix of the i^{th} element
$\boldsymbol{l}, \boldsymbol{p}, \boldsymbol{n}$	Unit vectors defining the local reference system
$\boldsymbol{C}$	Global coordinates of the element centroid
d	Element edge length
$\boldsymbol{c}$	Element edge mid-point
$\boldsymbol{J}$	Jacobian matrix

Bibliography

[1] K.-V. Yuen and G. A. Ortiz, "Outlier detection and robust regression for correlated data," *Comput. Methods Appl. Mech. Eng.*, vol. 313, pp. 632–646, 2017.

[2] A. Deraemaeker, E. Reynders, G. De Roeck, and J. Kullaa, "Vibration-based structural health monitoring using output-only measurements under changing environment," *Mech. Syst. Signal Process.*, vol. 22, no. 1, pp. 34–56, 2008.

[3] A. H. Alavi, H. Hasni, P. Jiao, W. Borchani, and N. Lajnef, "Fatigue cracking detection in steel bridge girders through a self-powered sensing concept," *J. Constr. Steel Res.*, vol. 128, pp. 19–38, 2017.

[4] C. R. Farrar and K. Worden, *Structural health monitoring: a machine learning perspective*. John Wiley & Sons, 2012.

[5] W. P. Leser, P. E. Leser, J. E. Warner, G. F. Bomarito, J. D. Hochhalter, and A. J. Newman, "A Computationally-Efficient Probabilistic Approach to Model-Based Damage Diagnosis," *Int. J. Progn. Heal. Manag.*, vol. 8, 2017.

[6] M. Corbetta, C. Sbarufatti, E. J. Cross, and M. Giglio, "Removal of temperature-induced strain variations for fatigue crack growth detection in a real aeronautical structure," in *8th European Workshop on Structural Health Monitoring, EWSHM 2016*, 2016, pp. 900–909.

[7] E. Figueiredo, G. Park, C. R. Farrar, K. Worden, and J. Figueiras, "Machine learning algorithms for damage detection under operational and environmental variability," *Struct. Heal. Monit.*, vol. 10, no. 6, pp. 559–572, 2011.

[8] S. Alampalli, "Effects of testing, analysis, damage, and environment on modal parameters," *Mech. Syst. Signal Process.*, vol. 14, no. 1, pp. 63–74, 2000.

[9] H. Sohn, "Effects of environmental and operational variability on structural health monitoring," *Philos. Trans. R. Soc. London A Math. Phys. Eng. Sci.*, vol. 365, no. 1851, pp. 539–560, 2007.

[10] B. Peeters and G. De Roeck, "One-year monitoring of the Z24-Bridge: environmental effects versus damage events," *Earthq. Eng. Struct. Dyn.*, vol. 30, no. 2, pp. 149–171, 2001.

[11] K. Worden, H. Sohn, and C. R. Farrar, "Novelty detection in a changing environment: regression and interpolation approaches," *J. Sound Vib.*, vol. 258, no. 4, pp. 741–761, 2002.

[12] C. P. Fritzen, G. Mengelkamp, and A. Guemes, "Elimination of temperature effects on damage detection within a smart structure concept," *Struct. Heal. Monit.*, vol. 10, pp. 15–17, 2003.

[13] K. Worden and E. J. Cross, "On switching response surface models, with applications to the structural health monitoring of bridges," *Mech. Syst. Signal Process.*, vol. 98, pp. 139–156, 2018.

[14] R. Ruotolo and C. Surace, “Damage detection using singular value decomposition,” in *DAMAS 97*, 1997.

[15] A.-M. Yan, G. Kerschen, P. De Boe, and J.-C. Golinval, “Structural damage diagnosis under varying environmental conditions - Part II: Local PCA for non-linear cases,” *Mech. Syst. Signal Process.*, vol. 19, no. 4, pp. 865–880, 2005.

[16] H. Sohn, K. Worden, and C. R. Farrar, “Statistical damage classification under changing environmental and operational conditions,” *J. Intell. Mater. Syst. Struct.*, vol. 13, no. 9, pp. 561–574, 2002.

[17] J. Kullaa, “Is temperature measurement essential in structural health monitoring,” in *Proc. 4th Int. Workshop on Structural Health Monitoring, Stanford University, CA*, 2003, pp. 717–724.

[18] E. J. Cross, K. Worden, and Q. Chen, “Cointegration: a novel approach for the removal of environmental trends in structural health monitoring data,” in *Proceedings of the Royal Society of London A: Mathematical, Physical and Engineering Sciences*, 2011, vol. 467, no. 2133, pp. 2712–2732.

[19] H. Shi, K. Worden, and E. J. Cross, “A regime-switching cointegration approach for removing environmental and operational variations in structural health monitoring,” *Mech. Syst. Signal Process.*, vol. 103, pp. 381–397, 2018.

[20] S. J. Wildy, A. G. Kotousov, and J. D. Codrington, “A new passive defect detection technique based on the principle of strain compatibility,” *Smart Mater. Struct.*, vol. 17, no. 4, p. 45004, 2008.

[21] S. Wildy, B. Cazzolato, and A. G. Kotousov, “Detection of delamination damage in a composite laminate beam utilising the principle of strain compatibility,” in *Key Engineering Materials*, 2010, vol. 417, pp. 269–272.

[22] S. Wildy and J. Codrington, “An Algorithm for Identifying a Crack Within a Measured Displacement Field,” *J. Nondestruct. Eval.*, vol. 36, no. 2, p. 37, 2017.

[23] A. Tessler and J. L. Spangler, “A variational principle for reconstruction of elastic deformations in shear deformable plates and shells,” *NASA/TM-2003-212445*, 2003.

[24] A. Tessler and J. L. Spangler, “Inverse FEM for full-field reconstruction of elastic deformations in shear deformable plates and shells,” in *2nd European Workshop on Structural Health Monitoring; 7-9 Jul. 2004; Munich; Germany*, 2004.

[25] P. Cerracchio, M. Gherlone, and A. Tessler, “Real-time displacement monitoring of a composite stiffened panel subjected to mechanical and thermal loads,” *Meccanica*, vol. 50, no. 10, pp. 2487–2496, 2015.

[26] M. Gherlone, P. Cerracchio, and M. Mattone, “Shape sensing methods: Review and experimental comparison on a wing-shaped plate,” *Prog. Aerosp. Sci.*, vol. 99, pp. 14–26, 2018.

[27] A. Kefal and E. Oterkus, “Shape sensing of aerospace structures toward coupling of isogeometric analysis and inverse finite element method,” in *58th AIAA/ASCE/AHS/ASC Structures, Structural Dynamics, and Materials Conference, 2017*, 2017.

[28] U. Papa, S. Russo, A. Lamboglia, G. Del Core, and G. Iannuzzo, “Health structure monitoring for the design of an innovative UAS fixed wing through inverse finite element method (iFEM),” *Aerosp. Sci. Technol.*, vol. 69, pp. 439–448, 2017.

[29] A. Kefal, A. Tessler, and E. Oterkus, “An enhanced inverse finite element method for displacement and stress monitoring of multilayered composite and sandwich structures,” *Compos. Struct.*, vol. 179, pp. 514–540, 2017.

[30] A. Kefal and E. Oterkus, “Displacement and stress monitoring of a chemical tanker based on inverse finite element method,” *Ocean Eng.*, vol. 112, pp. 33–46, 2016.

[31] M. Alioli, P. Masarati, M. Morandini, T. Carpenter, N. B. Osterberg, and R. Albertani, “Membrane shape and transverse load reconstruction using inverse fem,” in *Proceedings of the ASME Design Engineering Technical Conference*, 2015, vol. 6.

[32] P. Cerracchio, M. Gherlone, M. Di Sciuva, and A. Tessler, “Shape and stress sensing of multilayered composite and sandwich structures using an inverse finite element method,” *Int. J. Solids Struct.*, vol. 49, pp. 3100–3112, 2013.

[33] A. Kefal, E. Oterkus, A. Tessler, and J. L. Spangler, “A quadrilateral inverse-shell element with drilling degrees of freedom for shape sensing and structural health monitoring,” *Eng. Sci. Technol. an Int. J.*, vol. 19, no. 3, pp. 1299–1313, 2016.

[34] A. Kefal and M. Yildiz, “Modeling of sensor placement strategy for shape sensing and structural health monitoring of a wing-shaped sandwich panel using inverse finite element method,” *Sensors (Switzerland)*, vol. 17, no. 12, 2017.

[35] M. Gherlone, P. Cerracchio, M. Mattone, M. Di Sciuva, and A. Tessler, “Beam shape sensing using inverse finite element method: theory and experimental validation,” in *Structural Health Monitoring 2011: Condition-Based Maintenance and Intelligent Structures - Proceedings of the 8th International Workshop on Structural Health Monitoring*, 2011, pp. 578–585.

[36] Y. Zhao, H. Bao, X. Duan, and H. Fang, “The Application Research of Inverse Finite Element Method for Frame Deformation Estimation,” *Int. J. Aerosp. Eng.*, vol. 2017, 2017.

[37] X. Song and D. Liang, “Dynamic displacement prediction of beam structures using fiber bragg grating sensors,” *Optik (Stuttg).*, vol. 158, pp. 1410–1416, 2018.

[38] M. Gherlone, P. Cerracchio, M. Mattone, M. Di Sciuva, and A. Tessler, “Shape sensing of 3D frame structures using an inverse finite element method,” *Int. J. Solids Struct.*, vol. 49, no. 22, pp. 3100–3112, 2012.

[39] M. Gherlone, P. Cerracchio, M. Mattone, M. Di Sciuva, and A. Tessler, “An inverse finite element method for beam shape sensing: theoretical framework and experimental validation,” *Smart Mater. Struct.*, vol. 23, no. 4, p. 45027, 2014.

[40] C. Sbarufatti and M. Giglio, “Performance qualification of an on-board model-based diagnostic system for fatigue crack monitoring,” *J. Am. Helicopter Soc.*, vol. 62, no. 4, pp. 1–10, 2017.

[41] C. E. Katsikeros and G. N. Labeas, “Development and validation of a strain-based structural health monitoring system,” *Mech. Syst. Signal Process.*, vol. 23, no. 2, pp. 372–383, 2009.

[42] C. Quach, S. Vazquez, A. Tessler, J. Moore, E. Cooper, and J. Spangler, “Structural anomaly detection using fiber optic sensors and inverse finite element method,” in *AIAA Guidance, Navigation, and Control Conference and Exhibit*, 2005, p. 6357.

[43] A. Tessler and J. L. Spangler, “A least-squares variational method for full-field reconstruction of elastic deformations in shear-deformable plates and shells,” *Comput. Methods Appl. Mech. Eng.*, vol. 194, no. 2–5, pp. 327–339, 2005.

[44] B. Zhang and S. Yu, “Identification of moving sinusoidal wave loads for sensor structural configuration by finite element inverse method,” in *IOP Conference Series: Materials Science and Engineering*, 2018, vol. 339, no. 1.

[45] A. Kefal and E. Oterkus, “Displacement and stress monitoring of a Panamax containership using inverse finite element method,” *Ocean Eng.*, vol. 119, pp. 16–29, 2016.

[46] R. D. Cook, “Four-node ‘flat’shell element: drilling degrees of freedom, membrane-bending coupling, warped geometry, and behavior,” *Comput. Struct.*, vol. 50, no. 4, pp. 549–555, 1994.

[47] A. Tessler and T. J. R. Hughes, “An improved treatment of transverse shear in the Mindlin-type four-node quadrilateral element,” *Comput. Methods Appl. Mech. Eng.*, vol. 39, no. 3, pp. 311–335, 1983.

[48] A. Tessler, H. Riggs, and M. Dambach, “A novel four-node quadrilateral smoothing element for stress enhancement and error estimation,” in *39th AIAA/ASME/ASCE/AHS/ASC Structures, Structural Dynamics, and Materials Conference and Exhibit*, 1998, p. 1713.

[49] A. Tessler, H. R. Riggs, C. E. Freese, and G. M. Cook, “An improved variational method for finite element stress recovery and a posteriori error estimation,” *Comput. Methods Appl. Mech. Eng.*, vol. 155, no. 1–2, pp. 15–30, 1998.

[50] G. T. Mase, R. E. Smelser, and G. E. Mase, *Continuum mechanics for engineers*. CRC press, 2009.

[51] A. Kefal, J. B. Mayang, E. Oterkus, and M. Yildiz, “Three dimensional shape and stress monitoring of bulk carriers based on iFEM methodology,” *Ocean Eng.*, vol. 147, pp. 256–267, 2018.

[52] F. Mustapha, K. Worden, S. G. Pierce, and G. Manson, “Damage detection using stress waves and multivariate statistics: an experimental case study of an aircraft component,” *Strain*, vol. 43, no. 1, pp. 47–53, 2007.

[53] A. Tessler, “Structural analysis methods for structural health management of future aerospace vehicles,” in *Key Engineering Materials*, 2007, vol. 347, pp. 57–66.

[54] E. J. Miller, R. Manalo, and A. Tessler, “Full-Field Reconstruction of Structural Deformations and Loads from Measured Strain Data on a Wing Using the Inverse Finite Element Method,” *NASA/TM-2016-219407*, 2016.